cmgh
CELLULAR AND MOLECULAR GASTROENTEROLOGY AND HEPATOLOGY

ORIGINAL RESEARCH

FACI Is a Novel CREB-H–Induced Protein That Inhibits Intestinal Lipid Absorption and Reverses Diet-Induced Obesity

Yun Cheng,[1,2] Xiao-Zhuo Kang,[1,2] Tao Cheng,[1,2] Zi-Wei Ye,[3] George L. Tipoe,[1] Cheng-Han Yu,[1] Chi-Ming Wong,[4] Baohua Liu,[5] Chi-Ping Chan,[1,2] and Dong-Yan Jin[1,2]

[1]School of Biomedical Sciences, [2]State Key Laboratory of Liver Research, [3]Department of Microbiology, The University of Hong Kong, Pokfulam, Hong Kong; [4]Department of Health Technology and Informatics, The Hong Kong Polytechnic University, Hung Hom, Kowloon, Hong Kong; [5]Department of Biochemistry and Molecular Biology, Shenzhen University Health Science Center, Shenzhen, China

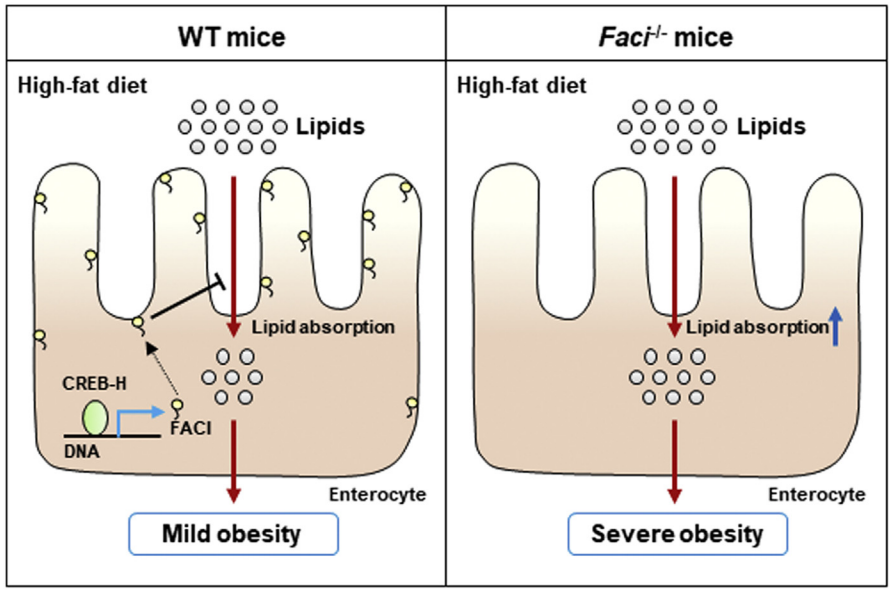

SUMMARY

CREB-H is a key regulator of lipid homeostasis. We identified fasting- and CREB-H–induced protein as a CREB-H–induced membrane and endosomal protein that binds to phospholipids. Using *Faci*-deficient mice, we defined a new function of fasting- and CREB-H–induced protein in the inhibition of intestinal lipid absorption and reversal of obesity.

BACKGROUND & AIMS: CREB-H is a key liver-enriched transcription factor governing lipid metabolism. Additional targets of CREB-H remain to be identified and characterized. Here, we identified a novel fasting- and CREB-H–induced (FACI) protein that inhibits intestinal lipid absorption and alleviates diet-induced obesity in mice.

METHODS: FACI was identified by reanalysis of existing transcriptomic data. *Faci*$^{-/-}$ mice were generated by clustered regularly interspaced short palindromic repeats (CRISPR)/CRISPR-associated 9 (Cas9)-mediated genome engineering. RNA sequencing was performed to identify differentially expressed genes in *Faci*$^{-/-}$ mice. Lipid accumulation in the villi was assessed by triglyceride measurement and Oil red O staining. In vitro fatty acid uptake assay was performed to verify in vivo findings.

RESULTS: FACI expression was enriched in liver and intestine. FACI is a phospholipid-binding protein that localizes to plasma membrane and recycling endosomes. Hepatic transcription of *Faci* was regulated by not only CREB-H, but also nutrient-responsive transcription factors sterol regulatory element-binding protein 1 (SREBP1), hepatocyte nuclear factor 4α (HNF4α), peroxisome proliferator-activated receptor γ coactivator-1α (PGC1α), and CREB, as well as fasting-related cyclic adenosine monophosphate (cAMP) signaling. Genetic knockout of *Faci* in mice showed an increase in intestinal fat absorption. In accordance with this, *Faci* deficiency aggravated high-fat diet–induced obesity, hyperlipidemia, steatosis, and other obesity-related metabolic dysfunction in mice.

CONCLUSIONS: FACI is a novel CREB-H–induced protein. Genetic disruption of *Faci* in mice showed its inhibitory effect on fat absorption and obesity. Our findings shed light on a new target of CREB-H implicated in lipid homeostasis. *(Cell Mol Gastroenterol Hepatol 2022;13:1365–1391; https://doi.org/10.1016/j.jcmgh.2022.01.017)*

Keywords: Lipid Homeostasis; Phospholipid-Binding Protein; Recycling Endosome; Intestinal Fat Absorption; Metabolic Syndrome.

See editorial on page 1469.

Lipids are key building blocks of the plasma membrane and other intracellular membrane structures. They are also vital to energy homeostasis, metabolism, and signal transduction. Diet ingestion is the major source of lipids in the human body. Excessive lipid ingestion is associated with an increased risk of obesity, hepatic steatosis, type 2 diabetes, and cardiovascular diseases.[1,2]

More than 95% of dietary fats are long-chain triglycerides (TGs), which are mainly digested and absorbed in the small intestine.[3] Within the small intestine, the ingested TGs are emulsified by bile acids and hydrolyzed into monoglycerides and free fatty acids (FFAs) by specific esterases. These digested lipids cross the intestinal mucosa either via passive diffusion or by protein-mediated transport mechanisms. The cytosolic FFAs are bound by fatty acid–binding proteins, and transported to endoplasmic reticulum (ER) and other organelles for further processing. In the ER, TGs are resynthesized by monoglycerides and FFAs through the monoacylglycerol pathway. Resynthesized TGs are either packaged into chylomicrons (CMs) for secretion or cytoplasmic lipid droplets as temporary storage. CMs are the main postprandial source of TGs for peripheral cells and tissues.[4–6]

In addition to the master transcription factor sterol regulatory-element binding protein (SREBP) that governs lipid metabolism, CREB-H is another ER membrane-bound transcription factor pivotally involved in the regulation of lipid metabolism.[7,8] *Crebh*$^{-/-}$ mice are hypertriglyceridemic.[9,10] CREB-H deficiency also results in familial hypertriglyceridemia, as seen in a subset of human patients.[11,12] CREB-H is expressed primarily in the liver and small intestine. Proteolytic activation of CREB-H releases an active form known as CREB-H–ΔTC, which translocates to the nucleus to activate the transcription of target genes including *Apoa4*, *Apoc2*, *Fgf21*, and *Cidec*, which mediate the effect of CREB-H on hepatic lipolysis, lipogenesis, fatty acid oxidation, as well as lipid droplet growth and fusion.[8,13] Intestinal overexpression of CREB-H has been found to suppress cholesterol absorption by preventing the expression of the *Npcl1* gene, which encodes a rate-limiting transporter of cholesterol.[14] In addition, intestine-specific knockout of *Crebh* in mice also results in augmentation of TG absorption from diet.[15] However, CREB-H target genes that specifically regulate intestinal TG absorption have not been identified.

Our previous analysis of CREB-H has provided evidence for its regulation of gluconeogenesis as well as the regulatory mechanism for its proteolytic activation and degradation.[10,16,17] Identification of additional CREB-H target genes might provide new clues to its physiological function in lipid homeostasis. To this end, we performed a comparative analysis of differentially expressed genes in the liver of wild-type (WT) and *Crebh*$^{-/-}$ mice by transcriptomics. Our analysis led to the identification of FLJ22675 or *C11orf86*, an uncharacterized novel target gene of CREB-H. Because it was found to be highly induced by fasting and CREB-H in our subsequent study, it was renamed fasting- and CREB-H–induced protein (FACI). In this study, we report on full characterization of FACI in terms of its CREB-H inducibility, expression profiles, subcellular localization to plasma membrane and recycling endosome, phospholipid-binding property, transcriptional regulation, and physiological function. In particular, *Faci*$^{-/-}$ mice showed enhanced intestinal TG absorption and diet-induced obesity.

Results

Faci Is a Novel CREB-H–Induced Gene Preferentially Expressed in Liver and Intestine

Transcriptome profiling of genes differentially expressed in the liver of Crebh WT and Crebh$^{-/-}$ mice has been available in 2 Gene Expression Omnibus (GEO) data sets.[9,18] Reanalysis of these data led to the identification of the *Faci* gene, which was underexpressed in Crebh$^{-/-}$ mice (Figure 1*A*). Indeed, the expression of *Faci* transcript in the liver of Crebh$^{-/-}$ mice was reduced substantially (Figure 1*B* and *C*). Consistent with this, pronounced induction of *Faci* messenger RNA (mRNA) was observed as the consequence of liver-specific transgenic expression of a constitutively active version of CREB-H, known as CREB-H-ΔTC, in Crebh$^{-/-}$ mice (Figure 1*D* and *E*). In addition, enforced expression of CREB-H–ΔTC and CREB-H–ΔTC–4A, which is a stabilized form of CREB-H,[17] robustly induced *Faci* mRNA expression in HepG2, Hep3B, and AML12 cells (Figure 1*F*, *H*, and *J*). HepG2 and Hep3B are 2 human hepatoma cell lines, whereas AML12 is a seemingly normal noncancerous hepatic cell line from mice.[19–21] Luciferase assay also confirmed potent activation of *Faci* promoter activity by CREB-H–ΔTC and CREB-H–ΔTC–4A (Figure 1*G*, *I*, and *K*).

Faci is a hypothetical protein-encoding gene with no known function. To verify that a protein can indeed be expressed from the *Faci* gene, 2 versions of mouse FACI

Abbreviations used in this paper: **AAV, adeno-associated virus; ANOVA, analysis of variance; AP, adaptor protein; BSA, bovine serum albumin; cAMP, cyclic adenosine monophosphate; CM, chylomicron; CR, conserved region; CREB-H, cAMP-responsive element-binding protein-hepatocyte; CRTC2, CREB regulated transcription coactivator 2; DEG, differentially expressed gene; DGAT, diglyceride acyltransferase; DMEM, Dulbecco's modified Eagle medium; Dox, doxycycline; EGFP, enhanced green fluorescent protein; ER, endoplasmic reticulum; FABP2, fatty acid-binding protein 2; FACI, fasting- and CREB-H–induced protein; FBS, fetal bovine serum; FFA, free fatty acid; GEO, Gene Expression Omnibus; HFD, high-fat diet; HNF4α, hepatocyte nuclear factor 4α; HRP, horseradish peroxidase; IDR, intrinsically disordered region; mRNA, messenger RNA; NCD, normal chow diet; PBS, phosphate-buffered saline; PGC1α, peroxisome proliferator-activated receptor γ coactivator 1α; PH, pleckstrin homology; rAAV, recombinant adeno-associated virus; Rab, Ras-related protein; RNA-seq, RNA sequencing; RT-qPCR, reverse-transcription quantitative polymerase chain reaction; SGK1, serum/glucocorticoid regulated kinase 1; SREBP, sterol regulatory element-binding protein; TG, triglyceride; WT, wild-type.**

Most current article

2352-345X
https://doi.org/10.1016/j.jcmgh.2022.01.017

proteins carrying an N-terminal V5 tag and a C-terminal 6xHis plus V5 (HisV5) tags were expressed transiently in HEK293T cells. V5-FACI and FACI-HisV5 protein bands of the predicted sizes of 15 and 16 kilodaltons were detected (Figure 1*L*, lanes 2, 4, and 5). A stabilizing effect of proteasome inhibitor MG132 on the V5-FACI protein (Figure 1*L*, lane 6 compared with lane 5) indicated that FACI likely undergoes proteasome-mediated degradation. Consistently, protein bands of V5-FACI and endogenous FACI of the expected sizes of 15 and 14 kilodaltons were detected in extracts of V5-FACI–overexpressing HEK293T cells and mouse liver, respectively (Figure 1*M*, lanes 1 and 3). Both bands disappeared with the addition of the immunizing peptide used to raise the rabbit antiserum (Figure 1*M*, lanes 2 and 4), lending support to the high specificity of our immunoblotting assay.

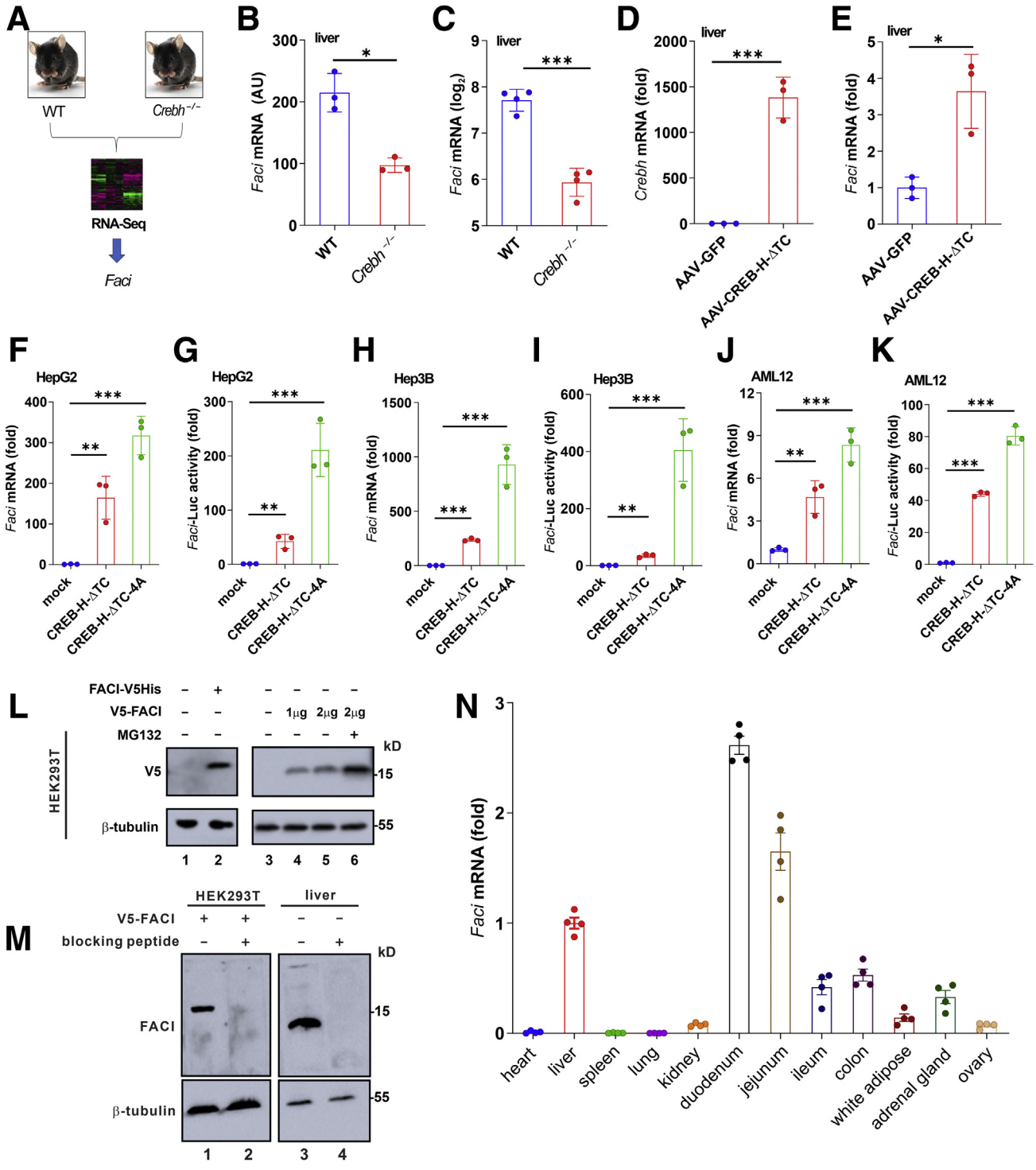

In general, agreement with the expression pattern of *Crebh*, reverse-transcription quantitative polymerase chain reaction (RT-qPCR) analysis showed enrichment of *Faci* mRNA in mouse liver and intestine (Figure 1*N*). In the intestine, the mRNA abundance of *Faci* decreased progressively from the duodenum to the colon (Figure 1*N*). In the liver, a single-cell RNA sequencing (RNA-seq) result[22] retrieved from the GEO database indicated that the *Faci* transcript was expressed primarily in hepatocytes, but not in other types of liver cells (Figure 2*A*). In the intestine, *Faci* mRNA was found predominantly in the epithelium (ie, villi and crypts) vs the mesenchyme as shown in the RNA-seq results from GEO (Figure 2*B*). This pattern was verified by our RT-qPCR analysis using isolated mouse intestinal epithelial cells and the remaining mesenchymal cells[23] (Figure 2*C*). Another 2 single-cell RNA-seq results[22,24] in GEO also indicated specific expression of *Faci* mRNA in enterocytes, but not in other types of epithelial cells in the intestine (Figure 2*D* and *E*). In particular, proximal and mature enterocytes in the small intestine showed higher expression of *Faci* mRNA than distal and immature ones. Hence, *Faci* is a hepatocyte- and enterocyte-enriched gene.

FACI does not contain any known functional domain. It is predicted to contain an N-terminal intrinsically disordered region and C-terminal α-helical regions (Figure 3*A*). Through alignment of all mammalian FACI protein sequences from Uniprot, we identified 5 conserved motifs designated A to E (Figure 3*B*). Interestingly, motif B (YxxL) matches the tyrosine-based sorting motif YxxΦ for adaptor protein 2 (AP2)-mediated endocytosis or adaptor protein 1 (AP1)-mediated transport.[25,26] Likewise, motif D (DxxLI) matches the acidic dileucine motif [DE]xxxL[LI], which is another sorting motif for AP2-mediated endocytosis or AP1-mediated transport.[25,26] Although records from NCBI Orthologs Database suggested the origin of the *faci* gene from reptiles, our protein sequence comparison revealed that the uncharacterized genes SB:CB 1058 in zebrafish and LOC115096979 in amphibians share 42.5% and 48.1% similarity with *faci* in turtles, respectively. SB:CB1058 and LOC115096979 also contain conserved C-terminal motif E, motif B (YxxL), and motif D (DxxLI) (Figure 3*B* and *D*). In addition, according to records from the Zebrafish Information Network, zebrafish SB:CB1058, similar to mouse *Faci*, is expressed mainly in liver and intestine. Thus, from the perspective of molecular evolution, the earliest FACI ortholog was found in zebrafish (Figure 3*C* and *D*). However, it is absent in snakes, crocodiles, or birds, and is likely lost in rabbits, but duplicates in pigs.

Localization of FACI to Plasma Membrane and Recycling Endosome

To analyze the subcellular localization of FACI, we established multiple AML12, Caco2, and Calu3 stable cell lines in which the expression of mEmerald-FACI or V5-FACI might be induced by doxycycline (Dox). Although Caco2 is a colorectal adenocarcinoma cell line, Calu3 is derived from human lung adenocarcinoma.[27,28] V5-FACI protein localized to the plasma membrane and a discrete cytoplasmic speckle in AML12 and Caco2 cells stably expressing V5-FACI protein (Figure 4*A*). The induction of V5-FACI expression in AML12-V5-FACI and Caco2-V5-FACI stable cells by Dox was verified by immunoblotting (Figure 4*B*). A similar localization pattern of mEmerald-FACI was observed independently in AML12 and Caco2 cells stably expressing mEmerald-FACI (Figure 4*C*).

To shed further light on the identity of FACI-containing cytoplasmic speckle, co-localization study was performed

Figure 1. (***See previous page***). ***Faci* is a CREB-H–regulated gene preferentially expressed in liver and intestine.** (*A*) Identification of *Faci* as a target of CREB-H. (*B* and *C*) *Faci* expression in the liver of WT and *Crebh*$^{-/-}$ mice. Data were retrieved from GEO data sets (*B*) GSE29643 and (*C*) GSE121096. Normalized mRNA expression intensities in arbitrary units (AU) for GSE29643 and $\log_2$ mRNA expression intensities for GSE121096 were statistically analyzed by the 2-tailed Student *t* test. (*D* and *E*) Verification of *Crebh* and *Faci* mRNA expression by RT-qPCR. Six-week-old *Crebh*$^{-/-}$ mice (male, n = 3 for each group) were injected intraperitoneally with AAV-green fluorescent protein (GFP) or AAV-CREB-H–ΔTC. AAV–CREB-H–ΔTC represents an AAV gene transfer vector expressing CREB-H–ΔTC driven by a liver-specific promoter and enhancers. Viral dose for injection was 1×10^{11} genome copies/mouse. After 2 weeks, mice were killed and total RNA in the liver was extracted to detect (*D*) *Crebh* and (*E*) *Faci* mRNA expression by RT-qPCR. The *Crebh* mRNA detected encodes CREB-H–ΔTC protein. The result was normalized to β-tubulin expression level. Data are means ± SD. Statistical significance was evaluated by the 2-tailed Student *t* test. (*F–K*) Induction of *Faci* mRNA expression or promoter activity by CREB-H–ΔTC. Expression levels of (*F*, *H*, and J) *Faci* mRNA or (*G*, *I* and *K*) relative *Faci*-Luc activity in (*F* and *G*) HepG2, (*H* and *I*) Hep3B, and (*J* and *K*) AML12 cells that are mock-transfected or transfected with CREB-H–ΔTC or CREB-H–ΔTC–4A plasmid were analyzed by RT-qPCR or luciferase reporter assay, respectively. The mRNA level was normalized to that of β-tubulin. The readout of firefly luciferase activity was normalized to that of Renilla luciferase. Statistical significance was evaluated by 1-way ANOVA with the Tukey post hoc tests. (*L*) FACI protein expression in transfected cells. HEK293T cells were transfected with plasmids encoding FACI-V5His and V5-FACI. Although FACI-V5His carries C-terminal tags, the V5 tag appears at the N-terminal of V5-FACI. Proteasome inhibitor MG132 was added to prevent protein degradation. (*M*) Expression of endogenous FACI protein. Polyclonal antiserum αFACI was raised in rabbits against a synthetic peptide of FACI. HEK293T cells transfected with V5-FACI plasmid (lanes 1 and 2) and mouse liver tissue (lanes 3 and 4) were harvested and lysed for protein extraction. Total protein samples were separated by sodium dodecyl sulfate–polyacrylamide gel electrophoresis and then probed with αFACI (lanes 1 and 3) and antibody-depleted αFACI (lanes 2 and 4). Antibody depletion was performed by pre-incubating αFACI for 2 hours with the synthetic peptide used as immunogen in antibody preparation. β-tubulin was detected as a loading control. (*N*) *Faci* mRNA expression profile in mouse tissues. Total RNA of indicated mouse tissues (n = 4) was extracted. The mRNA expression levels of *Faci* were analyzed by RT-qPCR and normalized to those of β-tubulin transcript. **P* < .05, ***P* < .01, and ****P* < .001.

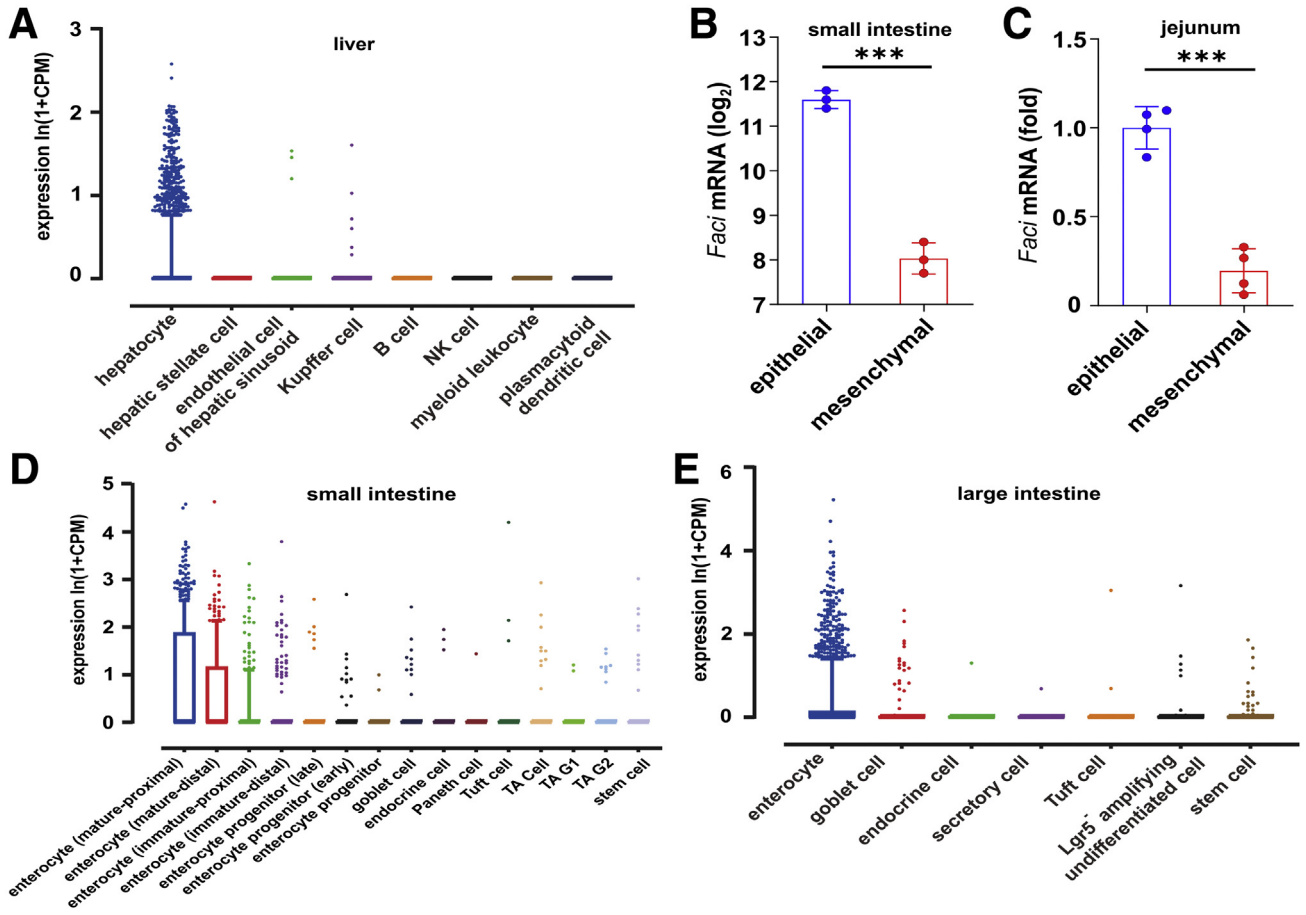

Figure 2. *Faci* is preferentially expressed in hepatocytes and enterocytes. (*A*) *Faci* mRNA expression in different cell clusters of liver. The single-cell RNA-seq data were retrieved from GEO: GSE109774. (*B*) *Faci* mRNA expression in mesenchymal and epithelial compartments of the developing intestine. The data were retrieved from GEO: GSE6383. Values represent $\log_2$ probe signal intensities. Statistical analysis was performed with the 2-tailed Student *t* test. (*C*) RT-qPCR analysis. Epithelial and mesenchymal compartments of the jejunum were isolated from mice (n = 4). The total RNA was extracted and *Faci* mRNA levels were analyzed by RT-qPCR. Relative mRNA expression levels were derived by normalizing to the levels of β-tubulin transcript. The 2-tailed Student *t* test was performed to judge statistical significance. Faci expression in different cell clusters of the (*D*) small intestine epithelium and (*E*) large intestine epithelium. The data on the small intestine epithelium were retrieved from GEO: GSE92332. The data on the large intestine epithelium were retrieved from GEO: GSE109774. ***$P < .001$. CPM, counts per million; NK, natural killer.

with different organellar markers including GM130 for Golgi apparatus, calreticulin-KDEL for ER, peroxisome-targeting signal 1 (PTS1) for peroxisome, MitoTracker (Invitrogen, Waltham, MA) for mitochondria, perilipin 2 (PLIN2) for lipid droplet, pleckstrin homology (PH) domain of FYVE for early endosome, Rab7a for late endosome, Ras-related protein 7A (Rab7A) for recycling endosome, Rab4 for early and sorting endosome that is rapidly recycling, lysosomal-associated membrane protein 1 (LAMP1) for lysosome, and microtubule-associated protein light chain 3 (LC3) for autophagosome.[29–35] FACI was found to co-localize perfectly with FYVE and Rab11a (Figure 4*D*). In contrast, FACI showed poor or no co-localization with other organellar markers, including Rab4 and Rab7a (Figures 4*D* and 5*A*). Thus, cytoplasmic FACI was concentrated in early endosomes and recycling endosomes, but almost absent from other organelles including late endosomes and fast recycling early endosomes. To further verify the subcellular localization of FACI, biochemical fractionation was conducted with lysates of AML12-V5-FACI cells. Consistent with confocal results, V5-FACI was enriched in the total membrane (plasma and organellar membranes) fraction, but not the cytosolic fraction (Figure 4*E*).

FACI is expressed mainly in hepatocytes and enterocytes in physiological conditions. Both are polarized epithelial cells, showing apical and basolateral sides. To determine whether the distribution of FACI in the plasma membrane at the apical and basolateral sides of polarized epithelial cells might differ, Caco2 and Calu3 cells stably expressing mEmerald-FACI were induced to differentiate into a polarized state. Z stacking then was used to show the fluorescent intensities of mEmerald-FACI at consecutive focal planes of the polarized cells. Although mEmerald-FACI was detected on both basolateral and apical plasma membranes in

polarized Calu3 and Caco2, the signal intensities of mEmerald-FACI, however, appeared to be much more prominent at the basolateral side when compared with those at the apical side (Figure 5*B*). Hence, FACI localizes to plasma membrane and recycling endosome ambiently, but it is more abundant in the basolateral plasma membrane.

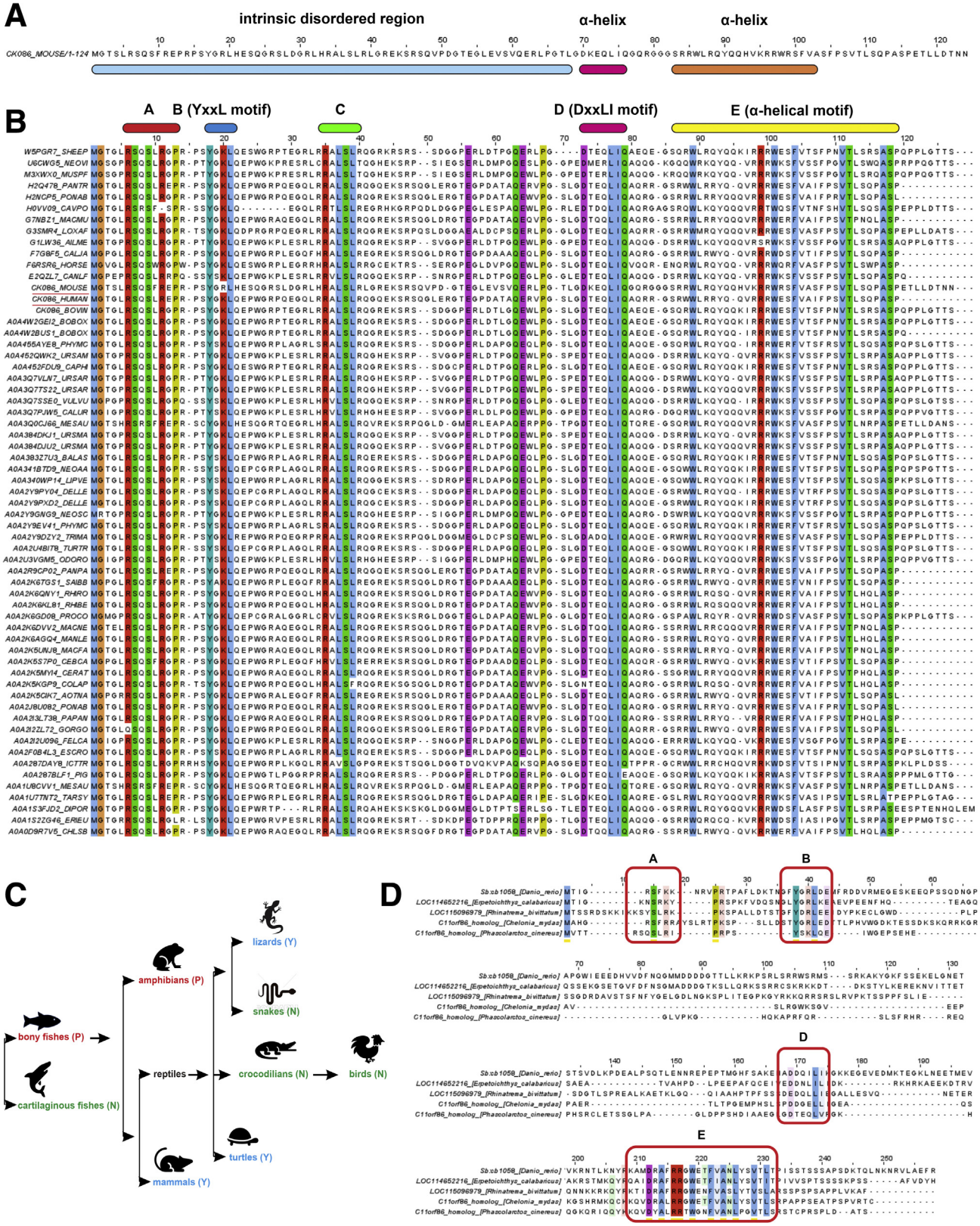

Membrane- and Phospholipid-Binding Property of FACI

FACI lacks a classic transmembrane domain but localizes to the plasma membrane. Both mEmerald-FACI and FACI-mEmerald proteins localized to the plasma membrane (Figures 4*C* and 6*A*), indicating that the membrane-binding property of FACI is not affected by the position of the mEmerald tag. To further characterize this property, a series of truncated FACI mutants (Figure 6*B*) were constructed. Mutants C and D of FACI harboring motif E showed the same localization pattern as that of the full-length FACI. In contrast, mutants A and B without motif E completely lost the localization to the plasma membrane (Figure 6*C*). Thus, plasma membrane localization is mediated by motif E. Motif E comprises the 22-amino acid long α-helix and its adjacent region. Further mutational analysis indicated the loss of plasma membrane localization in mutants E, F, and G of FACI, in which the long α-helix or its adjacent region is disrupted (Figure 6*C*). The plasma membrane localization pattern of mutant H lacking the second half of the α-helix–adjacent region, however, remained unchanged (Figure 6*C*). Hence, both the long α-helix and its immediate C-terminal residues are indispensable for localization of FACI to the plasma membrane. The mutational analysis also showed that motif E dictates the localization of FACI to early and recycling endosomes (Figure 6*C* and *D*).

The long α-helix within motif E was predicted to form an amphipathic helix (Figure 7*A*) by the HeliQuest program (https://heliquest.ipmc.cnrs.fr).[36] Because amphipathic helices are known to mediate protein binding to membranes and lipid surfaces,[37] we asked whether motif E could interact with lipids. A motif E–containing synthetic peptide comprising 77–115 amino acids of human FACI, designated FACI-C, was subjected to protein lipid overlay assay. FACI-C showed strong binding with PI4, $5P_2$, PI4P, PI3, 4, $5P_3$, and cardiolipin (Figure 7*B*). However, little or no binding was observed to other lipids and sphingolipids (Figure 7*B* and *C*). Further assessment of the binding affinity of FACI-C with different phosphoinositides through serial dilution indicated that FACI-C binds to PI4, $5P_2$, and PI3, $5P_2$ with high affinity; to PI3P, PI4P, PI5P, and PI3, 4, $5P_3$ with moderate affinity; and to PI3, $4P_2$, and PI with low affinity (Figure 7*D*).

The interaction between FACI and phosphoinositides was investigated further in cultured cells. Confocal and super-resolution images indicated substantial co-localization of FACI with mCherry-PLCD1-PH, a biosensor of PI4, $5P_2$,[38] but not with mCherry-TAPP-PH, a biosensor of PI3, $4P_2$[39] (Figure 7*E*). In addition, FACI also showed strong co-localization with enhanced green fluorescence protein (EGFP)-AKT-PH, a biosensor for PI3, 4, $5P_3$ and PI3, $4P_2$,[40] but not its dominant-negative version EGFP-AKT-PH (Figure 7*F*). Thus, FACI likely interacts with membrane by binding to membrane PI4, $5P_2$, and other phosphoinositides through its motif E, which contains an amphipathic helix.

Transcriptional Regulation of Faci

Mouse *Faci* and human *FACI* promoter regions were annotated based on database searching and bioinformatic analysis. Proximal to the transcription start site, 3 conserved regions named CR1, CR2, and CR3, were identified (Figure 8*A*). Because most putative regulatory elements are concentrated in the region starting from -400 bp to +80 bp, a DNA fragment corresponding to the region that covers -770 bp to +80 bp of human *FACI* promoter was cloned into pGL3-basic for promoter activity assay. A variety of transcription factors as well as protein kinases predicted to bind to *FACI* promoter or thought to be involved in the regulation of lipid homeostasis were tested for their effects on *FACI* transcription. Luciferase reporter assays were performed with CREB-H serving as a positive control. Liver- and intestine-enriched transcription factors SREBP1a[41] and HNF4α,[42] other transcription factors SREBP1c[41] and CREB,[43] as well as transcriptional coactivators CRTC2[44] and PGC1α[45] are potent activators of *FACI* promoter in HepG2 cells (Figure 8*B*). Although SREBP1a and SREBP1c are 2 isoforms of SREBP1, a master regulator of lipogenesis and cholesterol synthesis, CREB also is centrally involved in the regulation of glucose and lipid metabolism.[46] The regulation of *FACI* transcription by this combination of transcription factors is compatible with its role in lipid homeostasis.

We next mapped the responsive elements of the earlier-described transcriptional regulators in *FACI* promoter using 3 luciferase reporter constructs driven by progressively truncated *FACI* promoter regions designated pA, pB, and pC (Figure 8*C*). pB remained highly responsive to SREBP1a, SREBP1c, CREB-H, CREB, PGC1α, HNF4α, and CRTC2. Although pC had no response to SREBP1a, SREBP1c, CREB-H, or PGC1α, its response to CREB, HNF4α, and CRTC2 was attenuated (Figure 8*C*). Although SREBP1a, SREBP1c, HNF4α, and CRTC2 stimulated pA more robustly than pB, CREB and PGC1α activated pA and pB equally well (Figure 8*C*). These results were consistent with the requirement of the CR2 for the effects of all transcription

Figure 3. (***See previous page***). **FACI sequence alignment and phylogenetic analysis.** (*A*) Secondary structure prediction. Secondary structure of FACI was predicted using JPred (www.compbio.dundee.ac.uk/jpred) and IUPred2A (iupred2a.elte.hu). Two α-helical regions (red and orange) and 1 intrinsic disordered region (blue) are highlighted. (*B*) Multiple alignments of FACI homologs among 65 mammalian species. Five conserved regions are *boxed* and labeled as A to E. (*C*) A phylogenetic tree of FACI. FACI homologs exist in lizards, turtles, and mammals (blue), but are not found in cartilaginous fishes, snakes, crocodiles, or birds (green). Uncharacterized ancestral versions of FACI were identified in amphibians and bony fishes (red). (*D*) Sequence alignment of FACI homologs and ancestral forms. FACI homologs from Chelonia *mydas* (mammalia) and *Phascolarctos cinereus* (reptilia), as well as FACI ancestral proteins from *Rhinatrema bivittatum* (amphibia), *Erpetoichthys calabaricus* (osteichthyes), and *Danio rerio* (osteichthyes) were selected for analysis. Conserved motifs A, B, D, and E are *boxed*. N, species without FACI homologs; P, species with ancestral versions of FACI; Y, species with FACI homologs.

factors and regulators tested. The CR3 should contain specific regulatory elements for CREB, HNF4α, and CRTC2. Finally, the CR1 and AG repeat region should harbor cis-acting elements for SREBP1a, SREBP1c, CREB, HNF4α, and CRTC2, while the cis-acting elements for CREB and PGC1α might be located in the CR2.

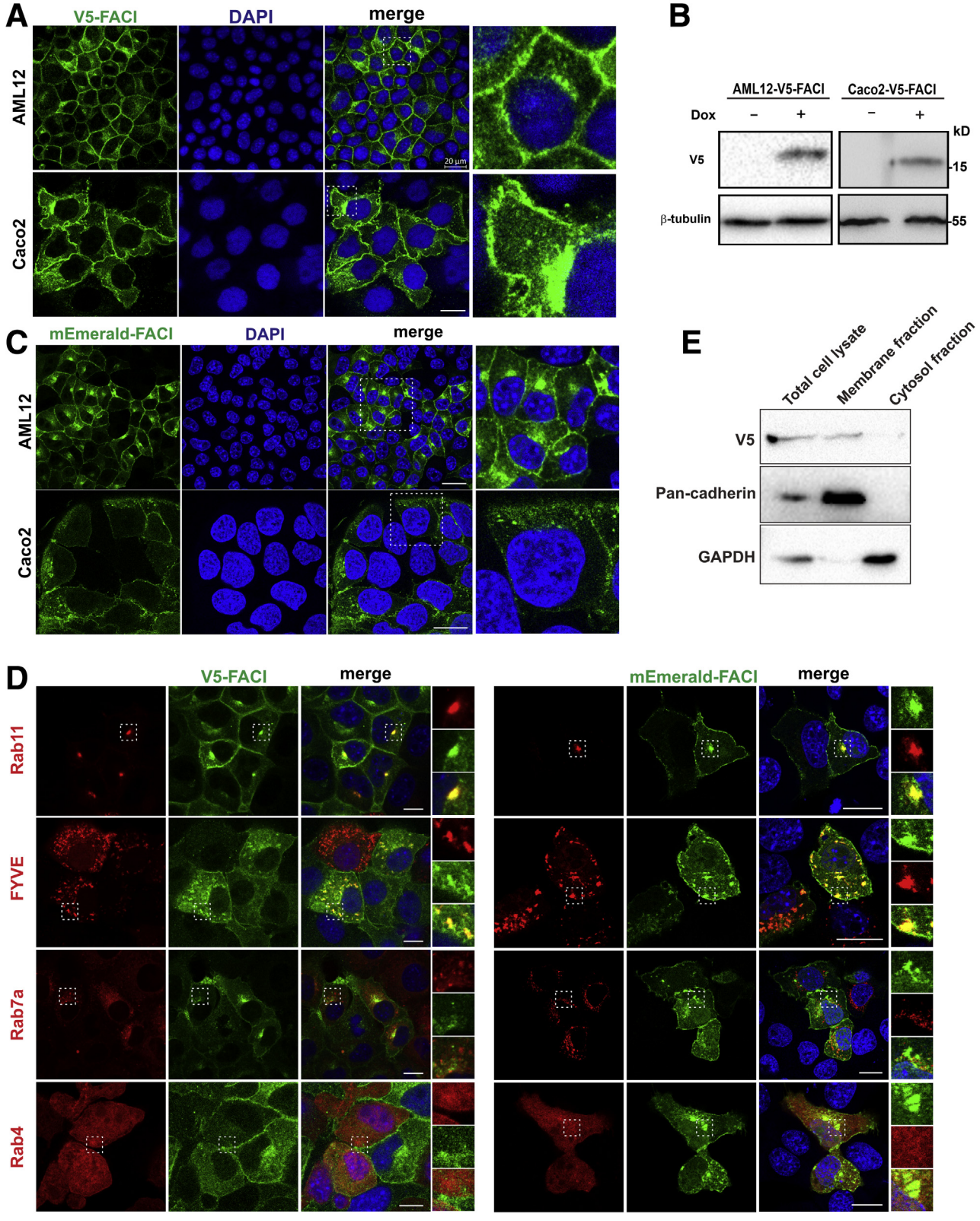

Because both CREB-H and CREB are induced by fasting,[46] we asked whether *Faci* transcription also might be induced by fasting. Indeed, hepatic expression of both *Faci* and *Crebh* mRNAs is robustly induced by fasting (Figure 8*D*). Likewise, *Faci* transcript also was upregulated by forskolin, a potent activator of CREB, CREB-H, and cAMP pathway, in gonadal adipose (Figure 8*E*). Consistent with this, transcription of human *FACI* gene in adipose tissue was potently induced by norepinephrine (Figure 8*F*), another stimulator of cAMP and CREB signaling.[47] Hence, *Faci* is regulated by multiple nutrient-related stimuli. Fasting and fasting-related cAMP signaling should be crucial in the induction of *Faci* mRNA expression in the liver and adipose tissue.

Faci Deficiency Aggravated Diet-Induced Obesity and Obesity-Related Metabolic Dysfunction in Mice

To investigate the in vivo function of FACI, we generated *Faci*$^{-/-}$ mice by clustered regularly interspaced short palindromic repeats (CRISPR)/CRISPR-associated 9 (Cas9) technology (Figure 9*A*). A DNA electrophoretogram verified complete removal of the *Faci* gene from the mouse genome (Figure 9*B*). RT-qPCR results further confirmed *Faci* knockout at the transcription level. Faci mRNA was undetectable in the liver and intestine of *Faci*$^{-/-}$ mice (Figure 9*C*). The deletion of the *Faci* gene was nonlethal and *Faci*$^{-/-}$ mice were normally developed. With the exception of a slight increase in body weight, which is discussed later (Figure 10*C* and *D*), we did not identify other overt abnormalities in *Faci*$^{-/-}$ mice.

The tissue distribution and transcriptional regulation of *Faci* suggested that *Faci* might affect energy hemostasis and particularly lipid metabolism. To explore this possibility, we challenged *Faci*$^{-/-}$ mice with a high-fat diet (HFD) and examined their metabolic changes under nutrient stress. The 8-week-old *Faci*$^{-/-}$ mice as well as their control littermates were fed with normal chow diet (NCD) or HFD for 12 weeks. After HFD feeding, both WT and *Faci*$^{-/-}$ mice showed increased body weight relative to NCD-fed mice (Figure 10*A* and *B*). However, HFD-fed *Faci*$^{-/-}$ (HFD-*Faci*$^{-/-}$) mice gained more weight than HFD-fed WT (HFD-WT) mice (Figure 10*A* and *B*). A slight increase in the body weight of *Faci*$^{-/-}$ mice in the absence of nutrient stress also was noted here (Figure 10*C* and *D*). In body composition analysis, HFD-*Faci*$^{-/-}$ mice showed higher percentages of fat mass compared with HFD-WT mice (Figure 10*E*). There was no significant difference in food intake between WT and *Faci*$^{-/-}$ mice (Figure 10*F and G*).

Dyslipidemia and hepatic steatosis were associated closely with obesity.[48] The effects of *Faci* deficiency on dyslipidemia and steatosis were examined. HFD-*Faci*$^{-/-}$ mice showed higher plasma cholesterol levels and slightly higher plasma TG levels than HFD-WT mice (Figure 10*H* and *I*). Compared with HFD-WT mice, HFD-*Faci*$^{-/-}$ mice showed an enlarged liver and increased liver weight and size on body weight ratio (Figure 10*J–L*). Plasma alanine aminotransferase levels of HFD-*Faci*$^{-/-}$ mice also were increased, indicative of more severe liver injury (Figure 10*M*). Liver cholesterol and TG levels also were increased in HFD-*Faci*$^{-/-}$ mice relative to HFD-WT mice (Figure 10*N* and *O*). H&E staining and Oil red O staining showed more severe hepatic lipid accumulation in HFD-*Faci*$^{-/-}$ mice (Figure 10*P*). Hence, HFD-*Faci*$^{-/-}$ mice developed more severe dyslipidemia and steatosis.

The impact of *Faci* deficiency on glucose homeostasis also was examined. HFD-*Faci*$^{-/-}$ mice showed more severe fasting hyperglycemia (Figure 11*A*) and fasting hyperinsulinemia (Figure 11*B*) than HFD-WT mice. In keeping with this, homeostasis model assessment of the insulin resistance index, a measure of insulin resistance, was increased significantly in HFD-*Faci*$^{-/-}$ mice (Figure 11*C*). An intraperitoneal glucose tolerance test further indicated worsened glucose tolerance in HFD-*Faci*$^{-/-}$ mice (Figure 11*D–G*). These findings suggested the development of more severe insulin resistance in *Faci*$^{-/-}$ mice under challenge with HFD.

Collectively, our results consistently showed aggravation of HFD-induced obesity as well as obesity-related steatosis, dyslipidemia, and insulin resistance in *Faci*$^{-/-}$ mice.

Enhanced TG Absorption in *Faci*$^{-/-}$ Mice

We speculated that abnormal intestinal TG absorption in *Faci*$^{-/-}$ mice might lead to its diet-induced obesity for 3 reasons. First, *Faci* is expressed most abundantly in the small intestine. Second, intestinal *Crebh* deficiency results in enhanced TG absorption plausibly through unknown targets. Third, the subcellular localization pattern, phospholipid-binding property, and transcriptional regulatory mechanism of FACI are compatible with its possible role in TG homeostasis. With these thoughts in mind, we compared intestinal epithelial transcriptomes of WT (n = 3) and *Faci*$^{-/-}$ mice (n = 3). Differentially expressed genes (DEGs) were selected with the criteria of a false discovery

Figure 4. (***See previous page***). **Subcellular localization of FACI.** (*A* and *C*) AML12 and Caco2 cell lines stably expressing (*A*) V5-FACI or (*C*) mEmerald-FACI were fixed and then subjected to either immunostaining followed by confocal microscopic analysis or confocal microscopic analysis directly. Nuclei were counterstained with 4′,6-diamidino-2-phenylindole (DAPI). FACI-mEmerald or V5-FACI is shown in green. (*B*) Immunoblotting. Expression of V5-FACI in AML2-V5-FACI and Caco2-V5-FACI stable cell lines was induced successfully by Dox. (*D*) AML12 cells were co-transfected with plasmids encoding V5-FACI or mEmerald-FACI plus 1 of the endosomal markers mCherry-Rab11a, mCherry-FYVE, mCherry-Rab7a, and Tag-RFP-Rab4a. Cells were fixed and subjected to either immunostaining followed by confocal microscopic analysis or confocal microscopic analysis directly. *Scale bars*: 20 μm. (*E*) Immunoblotting. Total membrane and cytosolic protein fractions of AML12-V5-FACI cells were isolated. V5-FACI was enriched in the total membrane fraction but not the cytosolic fraction. GAPDH, glyceraldehyde-3-phosphate dehydrogenase.

rate of less than 0.01 and a $\log_2$ fold change of not less than 1. The Pearson correlation coefficient analysis indicated a good positive correlation of all samples of either WT or *Faci*$^{-/-}$ mice (Figure 12*A*). A total of 17,676 genes were analyzed, of which 87 increased DEGs and 39 decreased DEGs were identified (Figure 12*B* and Supplementary Table 1). *Faci* was the most significantly down-regulated gene and its fragments per kilobase of transcript per

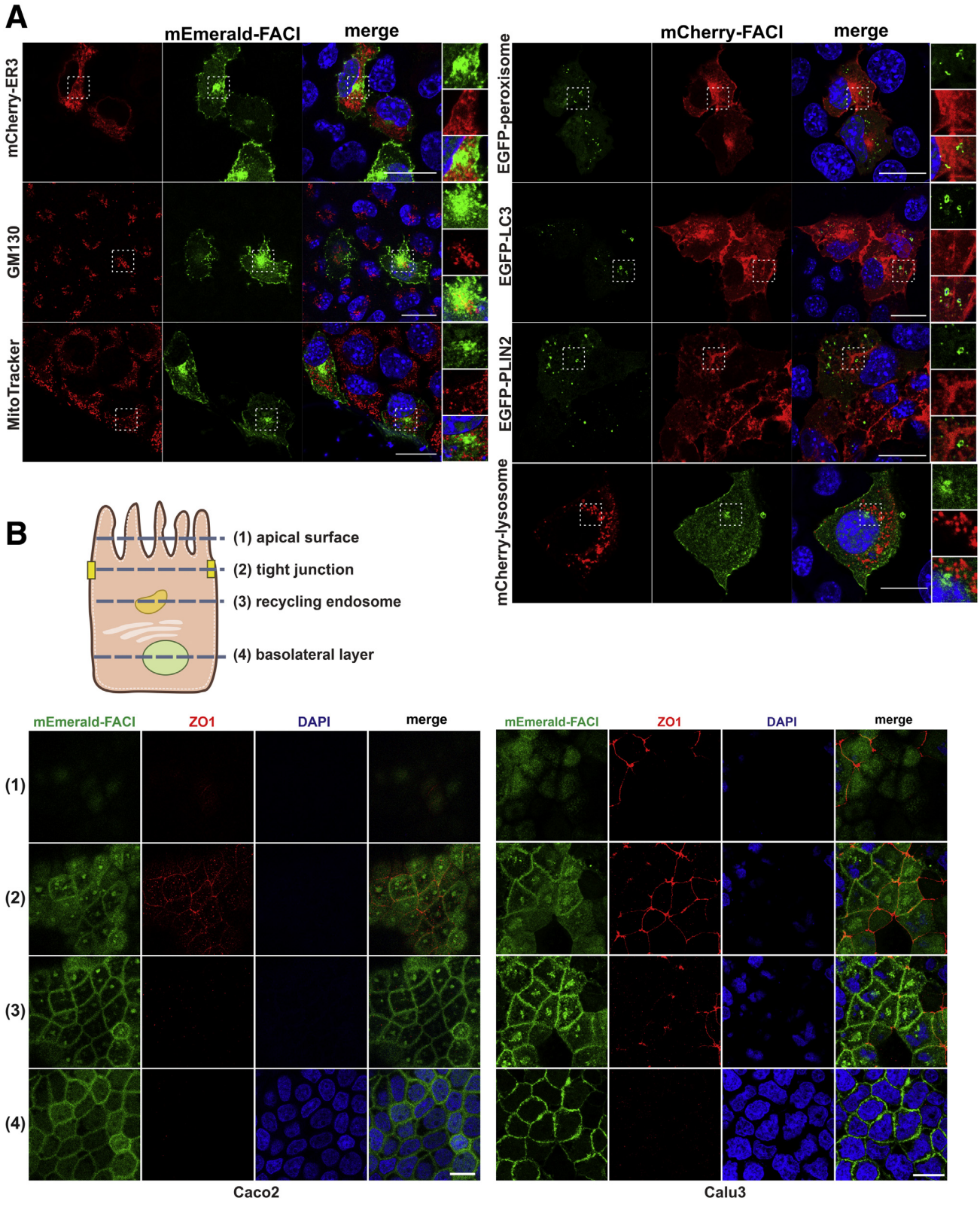

million mapped reads (FPKM) values in *Faci*$^{-/-}$ mice were undetectable (Figure 12*B* and Supplementary Table 2).

Gene ontology enrichment analysis of the up-regulated DEGs showed that the most relevant gene ontology terms included "brush border membrane," "response to nutrient," "cholesterol homeostasis," "phospholipid efflux," and "lipoprotein metabolic process" (Figure 12*C*). Plausibly, intestinal lipid homeostasis is affected by *Faci* deficiency. The enrichment analysis of the down-regulated DEGs, however, was not productive.

The up-regulated DEGs in *Faci*$^{-/-}$ mice included a number of lipid absorption–related genes (Figure 12*D* and Supplementary Table 1). Selected DEGs were verified by real-time RT-qPCR and immunoblotting. Expression of *Fabp2*, *Dgat2*, *Apob48*, *Apoc3*, and *Sgk1* mRNAs was increased in *Faci*$^{-/-}$ mice (Figure 12*E*). The steady-state levels of fatty acid-binding protein 2 (FABP2), diacylglycerol O-acyltransferase 2 (DGAT1), apolipoprotien B48 (APOB48), apolipoprotein C3 (APOC3), and serum/glucocorticoid regulated kinase 1 (SGK1) proteins also were increased in *Faci*$^{-/-}$ mice (Figure 12*F*). *Fabp2*, *Dgat2*, and *Apob48* are key genes that regulate lipid absorption.[5,49] SGK1 is a regulator of the absorption of not only glucose but also fatty acids.[50,51] Their increased expression in *Faci*$^{-/-}$ mice is suggestive of a possible role of FACI in intestinal lipid absorption.

The RNA-seq results prompted us to further explore whether *Faci* knockout might enhance intestinal fat absorption. We first compared the length and general morphology of the intestine between WT and *Faci*$^{-/-}$ mice. Neither the intestinal lengths nor the villi lengths of WT and *Faci*$^{-/-}$ mice showed obvious differences (Figure 12*G* and *H*). Fat absorption assays were performed next. *Faci*$^{-/-}$ mice showed increased plasma TG compared with WT mice after oil gavage (Figure 12*I*), indicating increased lipid absorption in *Faci*$^{-/-}$ mice. Because hepatic very-low-density lipoprotein–TG secretion was similar between WT and *Faci*$^{-/-}$ mice (Figure 12*J*), we could rule out potential interference with the assay by endogenous TG production. Furthermore, we observed enhanced postprandial lipid accumulation in the villi of *Faci*$^{-/-}$ mice by quantitative TG measurement (Figure 12*K*) and by Oil red O staining (Figure 12*L*). Consistent with this, Dox-induced expression of FACI in a Caco2 stable cell line (Figure 4*B*) significantly decreased the uptake of boron-dipyrromethene (BODIPY)-labeled C12 fatty acid (Figure 12*M* and *N*). Thus, although *Faci* knockout augmented intestinal fat absorption, expression of FACI showed the opposite effect.

Discussion

In this study we identified and characterized FACI, a novel target of CREB-H transcription factor. FACI is highly conserved among mammals and its expression is particularly enriched in liver and intestine (Figures 1–3). FACI localizes to plasma membrane and recycling endosomes, likely through its C-terminal amphipathic helix, which binds to phosphoinositides (Figures 4–7). FACI expression in the liver is regulated by nutrient-responsive transcription factors CREB-H, SREBP, HNF4α, CREB, and PGC1α (Figure 8), as well as fasting-related cAMP signaling. *Faci* deficiency in mice (Figure 9) exacerbated diet-induced obesity, hepatic steatosis, and dyslipidemia (Figures 10 and 11), which probably was caused by enhanced TG absorption (Figure 12). Our findings have implications in the therapeutic intervention of obesity and metabolic syndrome.

The structural properties of FACI suggest that it might be an integral monotopic protein or a peripheral membrane protein, which is attached to the inner leaflet of the plasma membrane and the outer leaflet of the endosomal membrane.[52] The C-terminal amphipathic α-helix domain of FACI mediates its binding with membrane phosphatidylinositol. The N-terminal region of FACI is a long intrinsically disordered region (IDR), comprising approximately two thirds of the protein (ie, 1–77 amino acids of mouse FACI). IDR refers to a protein region that does not fold into a fixed or unique 3-dimensional structure in its native state.[53] Thus, the N-terminal IDR of FACI might be string-like in the cytoplasm. However, after binding to macromolecules, the structural conformation of many IDRs can transit from fully disordered into stable globular states. Whether the IDR of FACI might follow this trend remains unknown.

FACI is a small protein with only approximately 115 amino acids. Except for the 5 conserved motifs, the other regions of FACI are disordered and evolutionarily more divergent. Plausibly, the 5 conserved motifs might be required for the execution of critical FACI functions. We have shown that motif E is responsible for membrane localization of FACI. The other 4 motifs seem to be functional short linear motifs. Short linear motifs generally are situated in IDRs, and act as interaction modules recognized by other biomolecules.[54] The sequence of motifs B (YXXL) and D (DXXXLI) just matches the sorting signals of adaptor complexes AP1 and AP2.[25] They plausibly mediate the trafficking of FACI between plasma membrane and endocytic vesicles. Online database PhosphoSitePlus (www.phosphosite.org) indicated that motifs A and C are phosphorylated. They have a similar sequence pattern of RXXpS,

Figure 5. (***See previous page***). **Further localization analysis of FACI.** (*A*) Co-localization of FACI with various organelle markers was examined. AML12 cells transiently expressing mEmerald-FACI (*left*) or mCherry-FACI (*right*) were probed or stained with various organellar markers including mCherry-ER3 for ER, GM130 for Golgi apparatus, MitoTracker for mitochondria, mCherry-lysosome for lysosome, EGFP peroxisome for peroxisome, EGFP-LC3 for autophagosome, and EGFP-PLIN2 for lipid droplets. Nuclei were stained with 4′,6-diamidino-2-phenylindole (DAPI). (*B*) Distribution of mEmerald-FACI in polarized Caco2 (*left*) and Calu3 (*right*) cells was examined. Caco2-mEmerald-FACI and Calu3-mEmerald-FACI stable cells were first differentiated into polarized states. Expression of mEmerald-FACI protein (green) then was induced with Dox. Representative Z-stack layers as indicated, including the apical layer, the layers with tight junction and recycling endosome, respectively, as well as the basal–lateral layer with nucleus, were imaged by confocal microscopy. Tight junction marker zonula occludens-1 (ZO-1) was stained with antibody and nucleus was stained with DAPI. *Scale bars*: 20 μm.

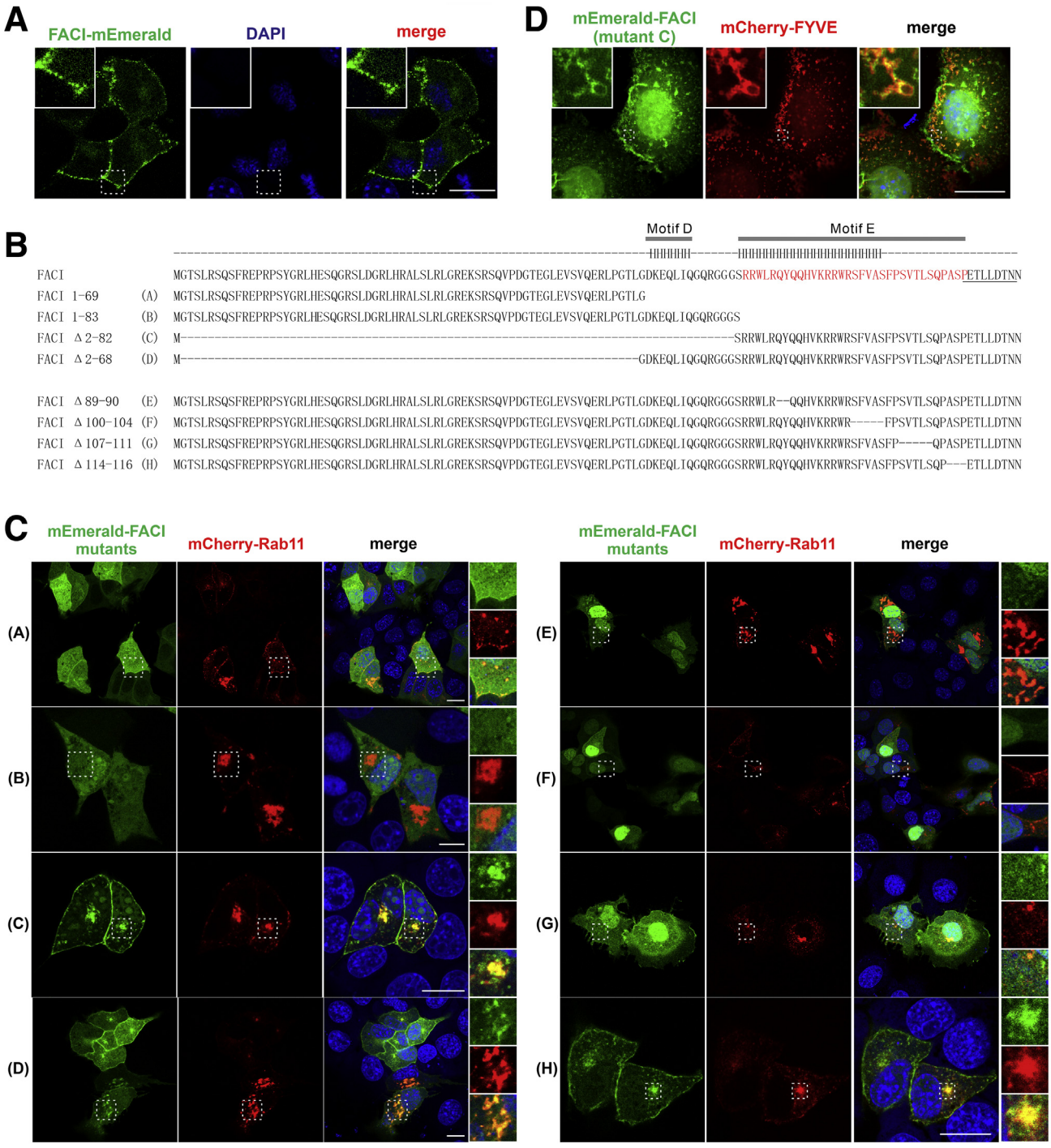

Figure 6. Determination of the membrane binding region of FACI. (*A*) Subcellular localization of FACI-mEmerald with C-terminal mEmerald. (*B*) A list of truncated FACI proteins. The region in red represents the conserved motif E. The α-helical regions within motif E were impaired in FACI-E and FACI-F mutants. The adjacent regions within motif E were disrupted in FACI-G and FACI-H mutants. The *underlined sequence* (ETLLDTNN) is present in mice but absent in human beings. (*C*) Co-localization analysis of FACI mutants with Rab11a. AML12 cells were transfected with plasmids expressing mCherry-Rab11a and the indicated mEmerald-FACI mutants. Cells were fixed and imaged by confocal microscopy. (*D*) Structured illumination imaging showing co-localization of mEmerald-FACI-mutant C, which contains motif E, with mCherry-FYVE in AML12 cells. *Scale bars*: 20 μm. DAPI, 4′,6-diamidino-2-phenylindole.

which matches the recognition site of AGC kinases.[55] Phosphorylation at these sites might serve key roles in the regulation of FACI function.

Proteins at the cell surface are dynamically regulated by endocytosis and endosomal recycling.[56] Under certain physiological conditions, such as ligand binding or

ubiquitination, proteins at the plasma membrane are internalized through clathrin-dependent and clathrin-independent endocytic pathways. Internalized proteins enter early endosomes for destination selection. Some proteins, such as ligand-activated cell surface receptors, are selected to the late endosome, and eventually to the lysosome for degradation, while other proteins, such as glucose, fatty acid, or amnio acid transporters, are sorted to the

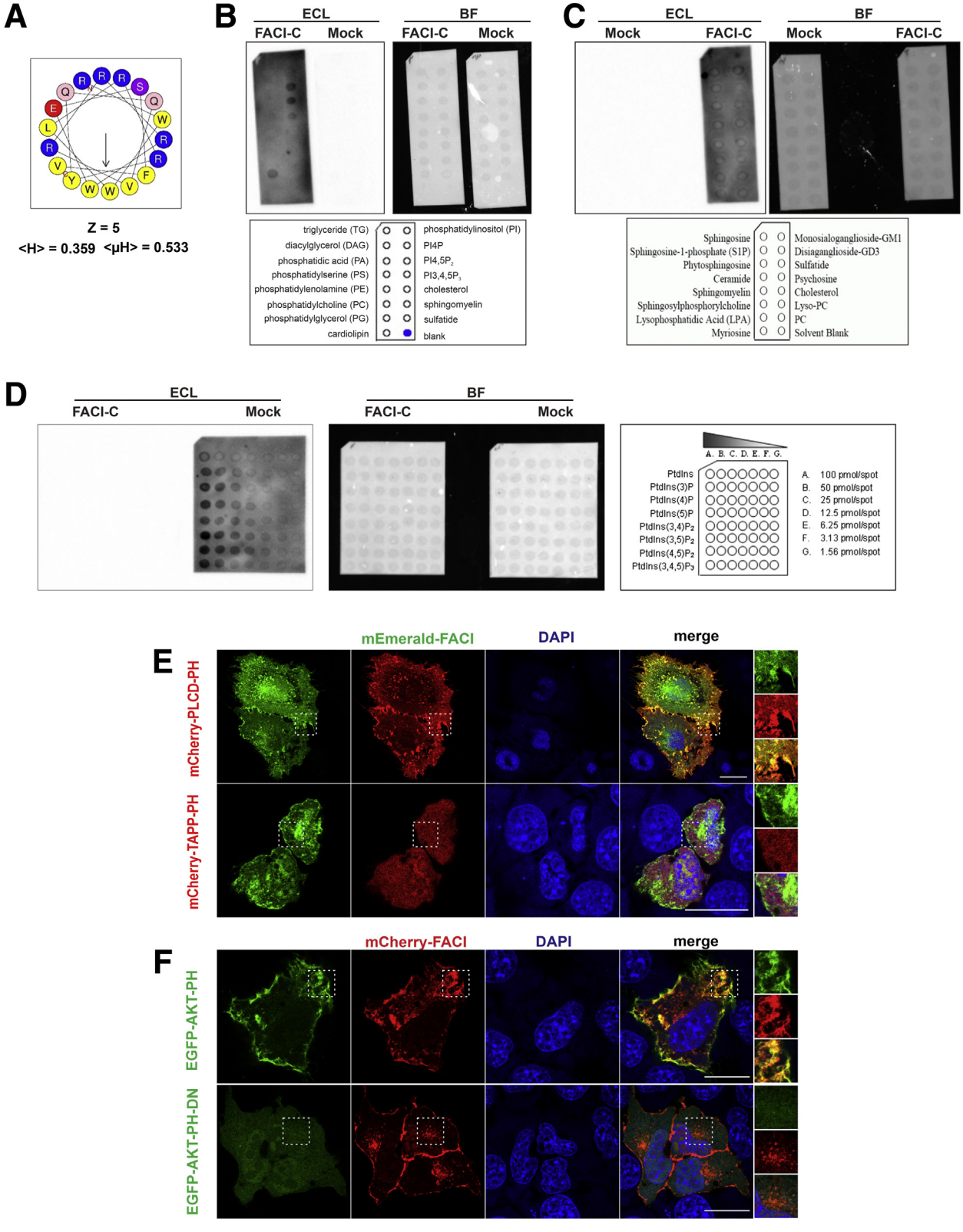

recycling endosome and finally recycled back to the plasma membrane.[57] FACI localizes primarily to the plasma membrane, early endosome, and recycling endosome, but it is almost absent from the late endosome, lysosome, and other organelles. Subcellular localization of FACI suggests a functional link to endocytosis and endosomal recycling. Considering that FACI affects intestinal lipid absorption, it probably serves to regulate endocytosis and/or recycling of membrane proteins such as lipid absorption–related transporters.

The tissue-specific expression and subcellular localization patterns of FACI as well as its transcriptional inducibility by CREB-H, SREBP, HNF4α, CREB, and PGC1α generally are consistent with the phenotypes of *Faci*$^{-/-}$ mice in intestinal lipid absorption. Plausibly, the nutrient-responsive transcription factors activate *Faci* transcription in the liver and intestine. Through its C-terminal amphipathic helix, FACI binds to selected phosphoinositides and thereby attaches to the plasma membrane and recycling endosome. Through an unknown mechanism, FACI impedes intestinal TG absorption, leading to reduced energy uptake. Ascribed to this property, FACI shows a protective effect on diet-induced obesity, hepatic steatosis, and dyslipidemia.

The mechanism by which FACI impedes intestinal lipid absorption remains to be clarified. In this regard, the following 3 possibilities warrant further investigations. First, the inhibition of fatty acid uptake by FACI (Figure 12) provides the impetus for further analysis of the impact of FACI on endocytosis or endosomal recycling of key fatty acid transporters. Fatty acid uptake across the apical membrane of the enterocyte is mediated mainly by protein transporters, such as CD36 and fatty acid transport protein 4 (FATP4).[2] FACI is localized to the plasma membrane and endocytic vesicles. FACI might affect endocytosis or endosomal recycling of fatty acid transporters, leading to lipid malabsorption. Second, the phospholipid-binding property of FACI (Figure 7) suggests a possible role of FACI in phospholipid remodeling, which requires further verification. Recent studies have indicated that fatty acid absorption is regulated by intestinal phospholipid remodeling.[58] It will be of interest to see whether FACI, as a phospholipid-binding protein, might affect fatty acid absorption by modulating membrane phospholipid composition. Third, the increased expression of FABP2, APOB, and APOC3 in *Faci*$^{-/-}$ mice (Figure 12) merits further functional characterization. FACI probably might affect fatty acid transport, CM package, and CM trafficking through these proteins.[6] The observation of APOB up-regulation in the intestine of *Faci*$^{-/-}$ mice is compatible with the activation of the CM pathway of fatty acid absorption. It will be of particularly great interest to see whether FACI might interact physically with APOB as well as other up-regulated proteins to modulate their function in intestinal lipid absorption.

The increased body weight of HFD-*Faci*$^{-/-}$ mice as well as the manifestation of insulin resistance, steatosis, and dyslipidemia (Figures 10 and 11) were caused at least in part by the enhanced TG absorption in the intestine (Figure 12). However, other potential reasons also may contribute to such phenotypes. We have indicated that SGK1 is up-regulated in the intestines of *Faci*$^{-/-}$ mice. SGK1 activation exacerbated diet-induced obesity, metabolic syndrome, and hypertension. Increased expression of intestinal SGK1 promoted glucose uptake by enhancing glucose transporter SGLT1 activity.[50,59] Therefore, increased SGK1 expression also partially may mediate diet-induced obesity as well as the metabolic syndrome of HFD-*Faci*$^{-/-}$ mice. On the other hand, abundant expression of FACI in hepatocytes (Figures 1 and 2) is suggestive of a potential hepatic function. Whether the absence of hepatic FACI exacerbates steatosis and insulin resistance in HFD-*Faci*$^{-/-}$ mice merits experimental validation.

Inhibitors of intestinal TG absorption have been developed as effective lipid-lowering drugs. Lomitapide, an inhibitor of microsomal triglyceride transfer (MTT) protein that is critical in intestinal TG absorption, has been approved for use as a lipid-lowering agent. Other MTT inhibitors such as JTT-130 and DGAT inhibitors such as PF-04620110 also have been tested extensively for potential use in the treatment of hypertriglyceridemia.[1,2,60] In this regard, FACI is a potential new target for therapeutic intervention. Agents that stabilize FACI or enhance its activity in intestinal lipid absorption might be further developed as lipid-lowering agents.

The increase in the hepatic cholesterol levels of HFD-*Faci*$^{-/-}$ mice (Figure 10) also is noteworthy. Intestine-specific *Crebh*$^{-/-}$ mice are known to have hypercholesterolemia attributed to enhanced cholesterol absorption as a result of increased expression of the *Npc1l1* gene.[1,2] Several questions concerning the impact of FACI on intestinal cholesterol absorption remain unanswered. First, it is not

Figure 7. (***See previous page***). **Phospholipid-binding property of FACI.** (*A*) Helical region in FACI. Amphipathic helices were identified in the C-terminus of FACI using Heliquest (heliquest.ipmc.cnrs.fr). The hydrophobic face is highlighted in yellow. The values of hydrophobic moment (<μH>), hydrophobicity (<H>), and net charge (Z) are indicated. (*B–D*) Fat blot assays. Synthetic peptide of 46 residues corresponding to the C-terminus of FACI (FACI-C) was biotin-labeled and incubated with the (*B*) Membrane Lipid Strip, (*C*) Sphingo Strip, and (*D*) MultiPIP Grip. HRP-conjugated streptavidin was used to visualize the biotin-labeled FACI-C peptide by enhanced chemiluminescence (ECL) reagents. Both ECL blot and bright field (BF) are shown. (*E*) Co-localization of FACI protein with phosphoinositides to plasma membrane. mEmerald-FACI plus PI4, $5P_2$ marker PLCD-PH or PI3, $4P_2$ marker TAPP-PH were expressed in AML12 cells. PLCD-PH or TAPP-PH is indicated in red, while FACI is indicated in green. For cells transfected with PLCD-PH, the plasma membrane layer was selected for confocal imaging. (*F*) AML12 cells were co-transfected with plasmids expressing mCherry-FACI and either AKT-PH or AKT-PH-dominant negative (DN). AKT-PH-DN is the dominant-negative form of AKT-PH. AKT-PH or AKT-PH-DN is shown in green. The red signals indicate FACI proteins. Nuclei were stained by 4′,6-diamidino-2-phenylindole (DAPI). Co-localization in the merged panels is shown in yellow. *Scale bars*: 20 μm.

known whether FACI also might inhibit intestinal cholesterol absorption. Second, it is intriguing whether the expression of *Npc1l1* mRNA also might be increased in *Faci*$^{-/-}$ mice. Finally, it remains to be elucidated whether FACI might affect the function of NPC1L1 in intestinal cholesterol absorption. Our ongoing studies focusing on

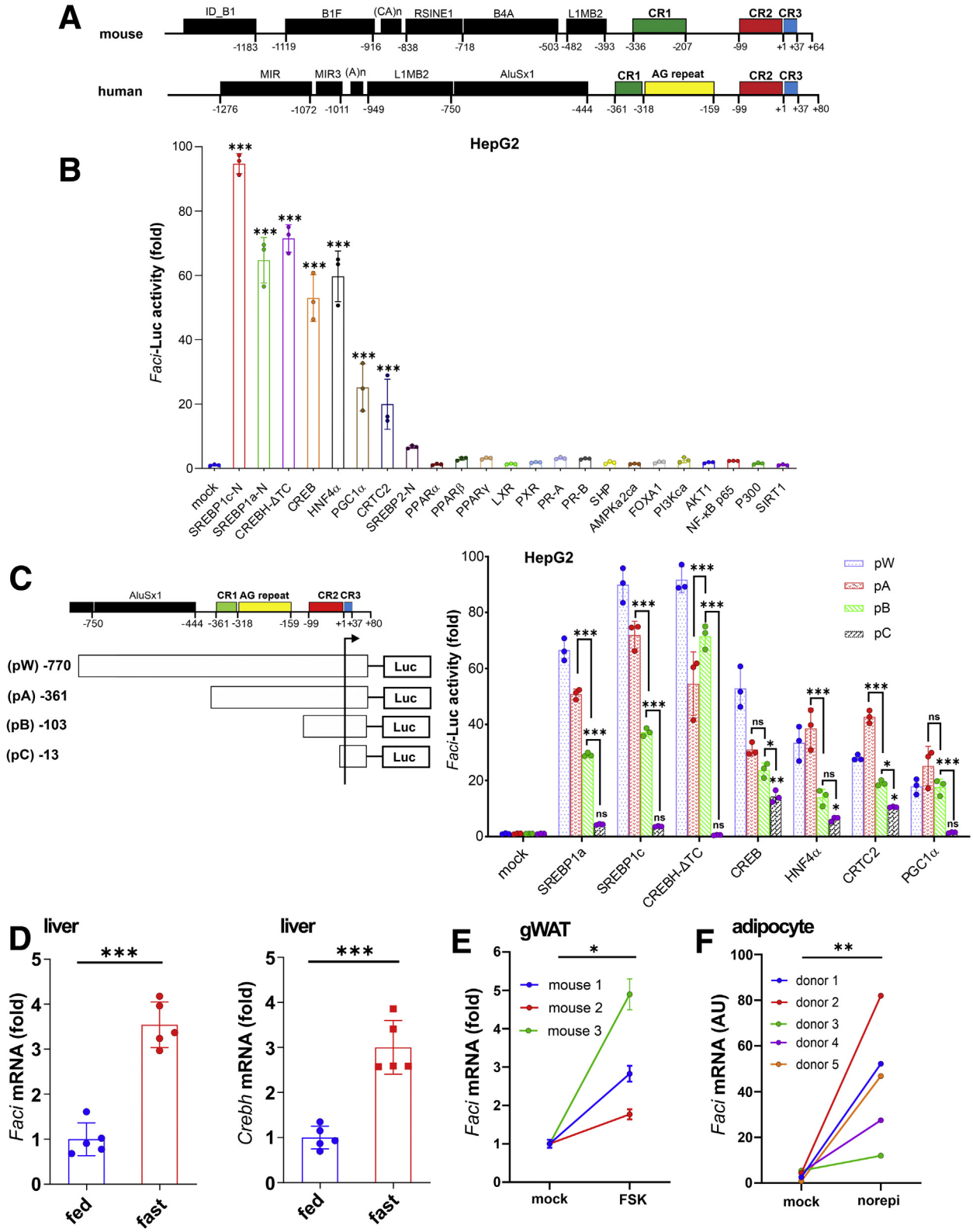

these questions will establish the role and therapeutic implications of FACI in cholesterol homeostasis.

Loss-of-function mutations of human *CREBH* locus have been identified in patients with familial hypertriglyceridemia.[11,12] Phenotypic changes of *Faci*$^{-/-}$ mice in lipid homeostasis include increased plasma TG, hepatic steatosis, and diet-induced obesity. In line with this, it will be of interest to see whether loss-of-function mutations of human *FACI* might be identified in patients with familial hypertriglyceridemia, hypercholesterolemia, and obesity. In addition to the function of FACI in lipid metabolism, bioinformatic analysis has shown abnormal expression of FACI in some other disease conditions. Ectopic high-expression of FACI was observed in lung adenocarcinoma and pancreatic adenocarcinoma, while FACI was underexpressed significantly in the intestine of patients with colon adenocarcinoma.[61] Genome-wide association studies also showed a close association of some single-nucleotide polymorphisms of *FACI* with familial lung cancer.[62] Further investigations also are required to elucidate the roles of FACI in the pathogenesis of these diseases.

Materials and Methods

Reagents, Plasmids, and Oligonucleotides

Reagents, plasmids,[63,64] primers, and single guide RNA (sgRNA) oligonucleotides for *Faci* gene knockout are listed in Supplementary Table 3.

Antibodies

Polyclonal rabbit anti-FACI antibodies were generated by custom antibody service of GenScript (Piscataway, NJ) using 1 synthetic FACI peptide as the immunogen. The peptide sequence is CTLGDKEQLIQGQRG, which is unique to mouse FACI. Commercial primary antibodies used in this study included mouse anti-V5 (Invitrogen Waltham, MA), mouse anti–β-tubulin (Sigma St. Louis, MO), mouse anti–β-actin (Sigma St. Louis, MO), mouse anti–zonula occludens-1 (ZO-1) (Thermo Fisher Waltham, MA), mouse anti-GM130 (BD Biosciences San Jose, CA), rabbit anti-APOB (Abcam Cambridge, United Kingdom), rabbit anti-FABP2 (Proteintech Rosemont, IL), rabbit anti-APOC3 (Abclonal Woburn, MA), mouse anti-DGAT2 (Santa Cruz), and mouse anti-SGK (Santa Cruz Dallas, TX). The secondary antibodies used included mouse IgG horseradish peroxidase (HRP)-linked whole antibody (Sigma St. Louis, MO) and rabbit IgG HRP-linked whole antibody (SigmaSt. Louis, MO). HRP-linked streptavidin was from Abcam. All antibody information has been listed in Supplementary Table 3.

Cell Culture and Transfection

Human hepatoma cell line Hep3B, human embryonic kidney cell line HEK293T, and human lung adenocarcinoma cell line Calu3 were cultured in Dulbecco's modified Eagle medium (DMEM) (ATCC Manassas, VA) containing 10% fetal bovine serum (FBS) (Life Technologies Carlsbad, CA). Human colorectal adenocarcinoma cell line Caco2 and human hepatoma cell line HepG2 were cultured in Eagle's minimum essential medium (ATCC Manassas, VA) containing 10% FBS. Mouse immortal hepatic cell line AML12 was cultured in DMEM/F12 medium (Gibco Waltham, MA) supplemented with insulin, transferrin, and selenium (Gibco), dexamethasone (Sigma), and 10% FBS. All cell lines were maintained at 37°C with a humidified atmosphere containing 5% CO_2.

HEK293T, HepG2, and Hep3B cells were transfected with GeneJuice transfection reagent (Novagen, Darmstadt, Germany). AML12 cells were transfected using Lipofectamine 3000 (Invitrogen Waltham, MA) with P3000 (Invitrogen Waltham, MA).

Differentiation of Caco2 and Calu-3

To induce epithelial polarity, Caco2 cells were plated and grown on 12-mm Transwells (Corning Corning, NY) for 21 days in DMEM with 10% FBS and 1% penicillin-streptomycin. Calu3 cells were plated and grown on 12-mm Transwells for 14 days in the same medium as for

Figure 8. (***See previous page***). **Transcriptional regulation of FACI.** (*A*) Schematic diagrams of the promoter regions of mouse *Faci* and human *FACI*. Conserved regions CR1 (green), CR2 (red), CR3 (blue), AG-repeat region (yellow), and the putative genomic repeat sequences (black) are highlighted. (*B*) Dual-luciferase reporter assay in HepG2 cells. Stimulatory effects on the *FACI* promoter were tested. HepG2 cells were co-transfected with pFACI-Luc (pW) and plasmids encoding the indicated transcription factors or transcriptional regulators. The readouts of firefly luciferase were measured and normalized to those of Renilla luciferase. Statistical significance for all groups was evaluated by 1-way ANOVA with the Dunnett post hoc tests. (*C*) Mutational analysis of *FACI* promoter. pGL3-basic reporter plasmids driven by 3 truncated versions of *FACI* promoter, designated pA, pB, and pC, were constructed (*left*). HepG2 cells were transfected with the indicated transcriptional regulators. The activities of pFACI-Luc (pW) and the 3 truncated versions (pA, pB, and pC) were measured. The readouts of firefly luciferase were measured and normalized to those of Renilla luciferase (*right*). Statistical significance was evaluated by 2-way ANOVA with the Tukey post hoc tests. $^{*}P < .05$, $^{**}P < .01$, and $^{***}P < .001$. The indicated groups were compared. The asterisks were placed directly on top of the error bars when the comparison was made with the mock. (*D*) *Faci* (*left*) and *Crebh* (*right*) mRNA expression in livers of fed and fasted mice. Mice with or without overnight fasting were killed and livers were collected for total RNA extraction. The mRNA expression level of *Faci* and *Crebh* were measured by RT-qPCR. Statistical analysis was performed with 2-tailed Student *t* test. $^{***}P < .001$. (*E*) Induction of *Faci* mRNA expression in gonadal white adipose tissue (gWAT) by forskolin (FSK). Adipose tissue explants from 3 male mice were mock-treated with vehicle or treated with forskolin for 2 hours. Total RNA was extracted and *Faci* mRNA expression was analyzed by RT-qPCR. $^{*}P < .05$ by 2-tailed paired Student *t* test. (*F*) Induction of *FACI* mRNA expression in human adipocytes by norepinephrine (norepi) treatment. Biopsy specimens from abdominal subcutaneous adipose tissue of nondiabetic human subjects were obtained. Differentiated adipocytes were stimulated for 4 hours with norepinephrine. Expression values represent transcripts per kilobase million. The data were retrieved from GEO: GSE150119. Statistical analysis was performed with 2-tailed Student *t* test. $^{**}P < .01$.

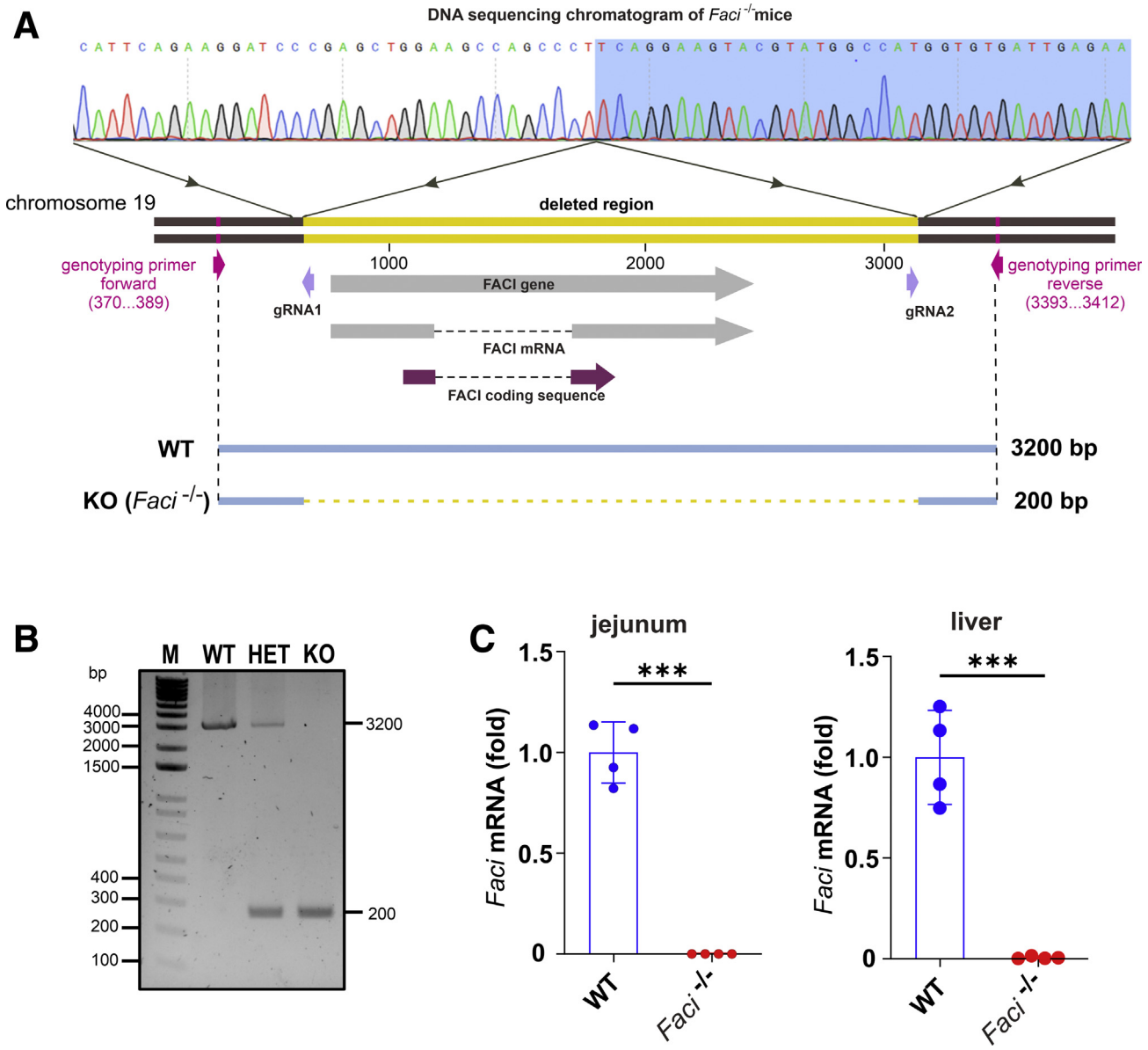

Figure 9. Generation and genotyping of *Faci*$^{-/-}$ mice. (*A*) Schematic diagram illustrating the strategy for generation of *Faci*$^{-/-}$ mice. Two gRNAs (gRNA1 and gRNA2) were designed for FACI knockout. Primers indicated were used for genotyping. A 3200-bp genotyping product was predicted for WT mice, while a 200-bp genotyping product was expected for *Faci*$^{-/-}$ mice. A DNA sequence chromatogram of *Faci*$^{-/-}$ mice also is shown. (*B*) Genotyping of *Faci*$^{-/-}$ mice. Genotyping PCR produced distinct products of 3200 bp for WT and 200 bp for *Faci*$^{-/-}$ mice. Both 3200-bp and 200-bp products were present in the heterozygous *Faci*$^{+/-}$ mice. (*C*) RT-qPCR analysis. Total mRNA of either intestinal epithelium from jejunum or liver of WT and *Faci*$^{-/-}$ mice (n = 4) was extracted. *Faci* mRNA expression was analyzed by RT-qPCR. *Faci* mRNA was undetectable in *Faci*$^{-/-}$ mice. ***$P < .001$ by unpaired 2-tailed Student *t* test. HET, heterozygous; KO, *Faci* knockout; M, DNA markers.

Caco2. The medium was changed daily through the culture duration for both cells.

Stable Cell Line Generation

Stable cell lines were generated with a lentiviral vector system using the protocol as described previously.[10] A total of 5 stable cell lines were established in this study, which are listed in Supplementary Table 3. Briefly, the lentiviral backbone vector was co-transfected into HEK293T cells with packaging constructs. After a 48-hour incubation, the culture medium was collected and filtered through a 0.22-μm filter. Virus-containing supernatant was concentrated further with Lenti-X Concentrator (Takara Kusatsu, Japan) and added to preseeded target cells with 8 μg/mL polybrene. The transduction was allowed for 48 hours, followed by puromycin selection to kill the lentivirus-negative cells.

Mice

C57BL/6 *Faci*$^{-/-}$ mice were generated with CRISPR/Cas9-mediated genome engineering by Cyagen (Santa Clara, CA).

Briefly, 2 gRNAs flanking the whole *Faci* gene were designed and transcribed in vitro. The gRNAs as well as the Cas9 protein were microinjected into fertilized oocytes to generate the founder mice. The founder mice were analyzed by genotyping and Sanger sequencing, and positive ones were backcrossed further with WT mice to generate $Faci^{+/-}$ heterozygotes. $Faci^{+/-}$ mice then were self-crossed to generate $Faci^{-/-}$ mice. $Faci^{-/-}$ mice have been backcrossed

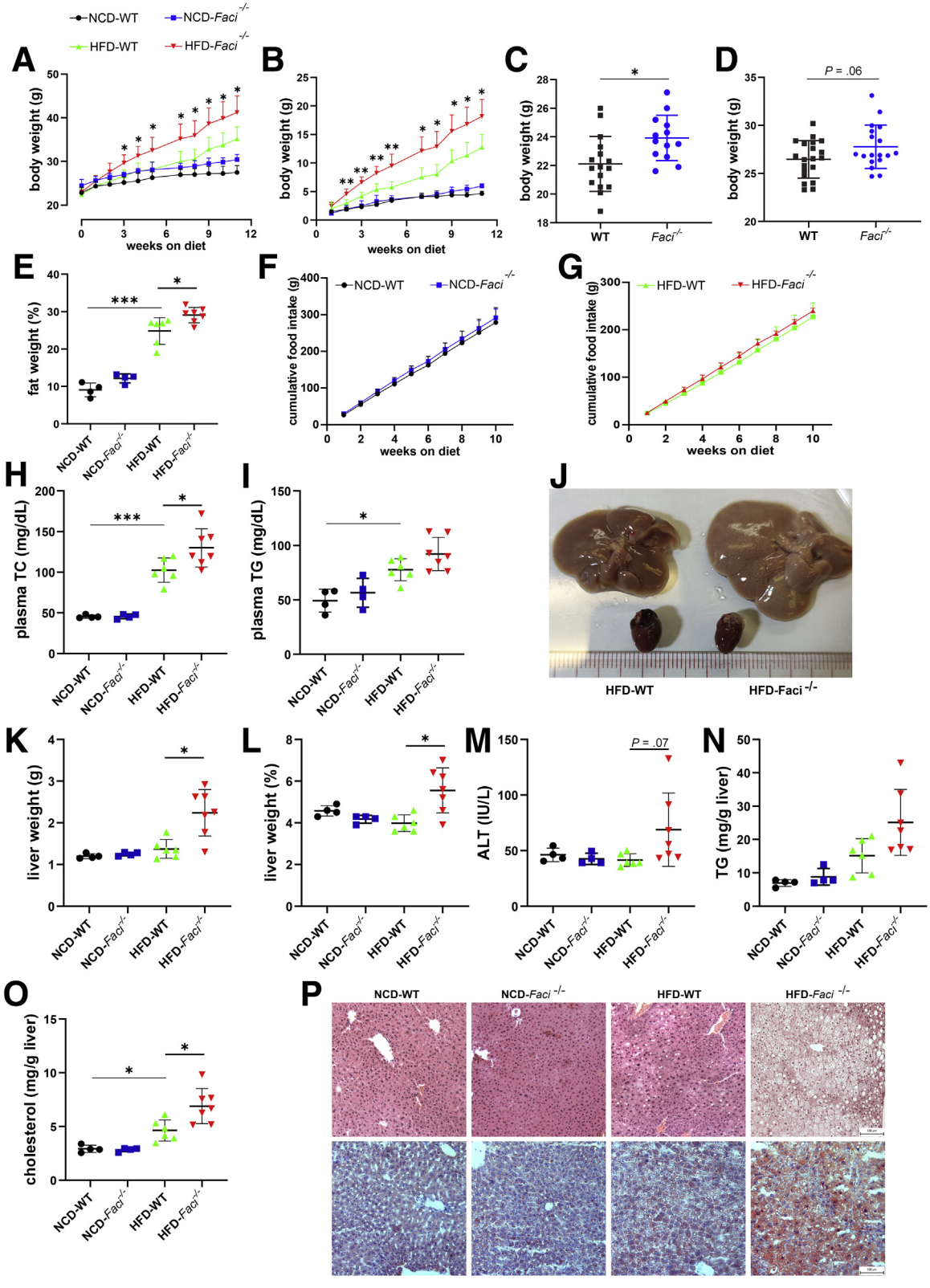

with C57BL/6 mice for 5 generations. Mice were housed in the Center for Comparative Medicine Research of the University of Hong Kong with a daylight cycle from 7 am to 7 pm. All animal experiments were approved by the Committee on the Use of Live Animals in Teaching and Research at the University of Hong Kong (Animal Ethics Approvals 3777-15 and 4776-18).

Adeno-Associated Virus–Mediated Transgene Expression In Vivo

The recombinant adeno-associated virus (AAV)2/8 system was used for in vivo liver-directed transgene expression.[65] Two recombinant AAVs (rAAVs) were generated in this study: a CREB-H–ΔTC–expressing rAAV (AAV-CREB-H-ΔTC) and an EGFP-expressing rAAV (AAV-EGFP) as control. The preparation and purification of rAAV have been described previously.[65] pLSP1-EGFP, from which EGFP expression is driven by a liver-specific human α1-antitrypsin promoter plus 2 copies of the human apolipoprotein enhancer or pLSP1–CREB-H–ΔTC was co-transfected with pXX6 and p5E18-VD2/8 at a ratio of 1:1:1 into the HEK293T cells for rAAV production. Viruses were harvested from infected cells 2 days after transfection by 4 freeze-thaw cycles. The rAAVs were purified further via cesium chloride gradient ultracentrifugation and the viral titers were determined by qPCR. For viral delivery, mice were injected intraperitoneally with rAAV with a dose of 1×10^{11} genome copy/mouse. After 2 weeks, mice were anesthetized, and liver tissues were collected for further assays.

Diets

Eight-week-old male WT and *Faci*$^{-/-}$ mice were acclimated in the treatment environment for 1 week before experiments. Mice were divided into 4 groups: WT mice fed with NCD (NCD-WT, n = 4), *Faci*$^{-/-}$ mice fed with NCD (NCD-*Faci*$^{-/-}$, n = 4), WT mice fed with high-fat diet (D12108C; Research Diets, New Brunswick, NJ) (HFD-WT, n = 6), and *Faci*$^{-/-}$ mice fed with a HFD (NCD-*Faci*$^{-/-}$, n = 7). Mice were fed ad libitum for 3 months. Food uptake and body weight were examined regularly. The body composition was examined spin echo magnetic resonance imaging.

Isolation of Intestinal Epithelium

Intestinal epithelium was isolated by the EDTA–dithiothreitol separation method.[66] Mice were killed and the small intestine was excised. The second one-sixth segment of the small intestine (jejunum) was collected and washed with cold phosphate-buffered saline (PBS) to flush off the feces. The intestine lumen was cut longitudinally and incubated in PBS with 30 mmol/L EDTA and 1.5 mmol/L dithiothreitol on ice for 20 minutes. The tissue then was incubated in 5 mL PBS with 30 mmol/L EDTA at 37°C for 10 minutes. After incubation, the epithelial cells were separated from the tissue by shaking the tube vigorously for 30 seconds 3 times. The epithelial cells were collected by centrifuging at 1000 $\times$ *g* for 5 minutes.

Forskolin Treatment

Mice were killed and the gonadal fat pads were excised. They were further cut into small pieces of 20 mg each and incubated in DMEM containing 2% fatty acid–free bovine serum albumin (BSA), with or without 10 μmol/L forskolin for 2 hours.

Blood Biochemistry Tests

All blood biochemistry tests were conducted following the manufacturer's instructions. Plasma insulin was measured by an enzyme-linked immunosorbent assay kit from Crystal Chem (Elk Grove Village, IL). Total TG, total cholesterol, and alanine aminotransferase were examined by kits from Stanbio (Kolkata, IN). Blood glucose was determined by glucometer Accu-Chek, Indianapolis, IN. Homeostasis model assessment of the insulin resistance index, a measure of insulin resistance, was calculated using the iHOMA2 software (Oxford, United Kingdom).[67]

Intraperitoneal Glucose Tolerance Test

Mice were fasted overnight before the assay. On the next day, mice were injected intraperitoneally with glucose (2 g/

Figure 10. (*See previous page*). *Faci* deficiency aggravates diet-induced obesity, dyslipidemia, and hepatic steatosis in mice. (*A*) Body weight and (*B*) weekly weight gain of male WT and *Faci*$^{-/-}$ mice on NCD or HFD diet (4 mice per NCD group, 6 mice per HFD-WT group, and 7 mice per HFD-*Faci*$^{-/-}$ group). Results are means ± SD. Statistical significance of body weights or weekly weight gain between HFD-WT and HFD-*Faci*$^{-/-}$ were assessed by 2-way ANOVA with repeated measures followed by the Tukey test. Body weight of (*C*) female and (*D*) male *Faci*$^{-/-}$ mice at 4 months. For this measurement, 18–20 female mice or 13–16 male mice were used in each group. *$P < .05$ by 2-tailed Student *t* test. (*E*) Fat percentages of male WT and *Faci*$^{-/-}$ mice on NCD or HFD diet for 11 weeks. Statistical analysis was performed with 1-way ANOVA with the Tukey post hoc test. (*F* and *G*) Cumulative food intake of male WT and *Faci*$^{-/-}$ mice on NCD or HFD diet. (*H* and *I*) Plasma (*H*) total cholesterol (TC) and (*I*) total TG levels of fasted male WT and *Faci*$^{-/-}$ mice on NCD or HFD diet for 12 weeks. Results were assessed statistically with 1-way ANOVA with the Tukey post hoc test. (*J*) Representative images of livers and hearts isolated from WT and *Faci*$^{-/-}$ mice on HFD diet for 12 weeks. (*K* and *L*) Liver weight and liver-weight percentages (liver weight/body weight) of WT and *Faci*$^{-/-}$ male mice on NCD or HFD diet for 12 weeks. Statistical analysis was performed with 1-way ANOVA with Welch correction followed by Games Howell post hoc tests. (*M*) Hepatic alanine aminotransferase (ALT) levels of male WT and *Faci*$^{-/-}$ mice on NCD or HFD diet for 12 weeks. Difference between HFD-WT and HFD-*Faci*$^{-/-}$ was assessed statistically with the Kruskal–Wallis test with the Dunn post hoc tests. (*N*) Hepatic TG and (*O*) cholesterol levels of male WT and *Faci*$^{-/-}$ mice on NCD or HFD diet for 12 weeks. Results were assessed statistically by 1-way ANOVA with Tukey post hoc tests. (*P*) Representative images of H&E-stained (*top row*) and Oil red O–stained (*bottom row*) liver sections from WT and *Faci*$^{-/-}$ mice on NCD or HFD diet for 12 weeks. *Scale bars*: 100 μm. *$P < .05$, **$P < .01$, and ***$P < .001$.

kg body weight), followed by examination of the blood glucose level using a glucometer at 0, 15, 30, 45, 60, 120, and 180 minutes after injection. Blood samples at the mentioned time points were collected and plasma insulin levels also were determined.

Very-Low-Density Lipoprotein Secretion Assay

Female WT and *Faci*$^{-/-}$ mice (n = 3 per group) were HFD-fed for 5 days, fasted overnight, and injected intraperitoneally with 30% wt/wt poloxamer 407 (Sigma-Aldrich) solution in PBS (1.5 g/kg body weight). Blood

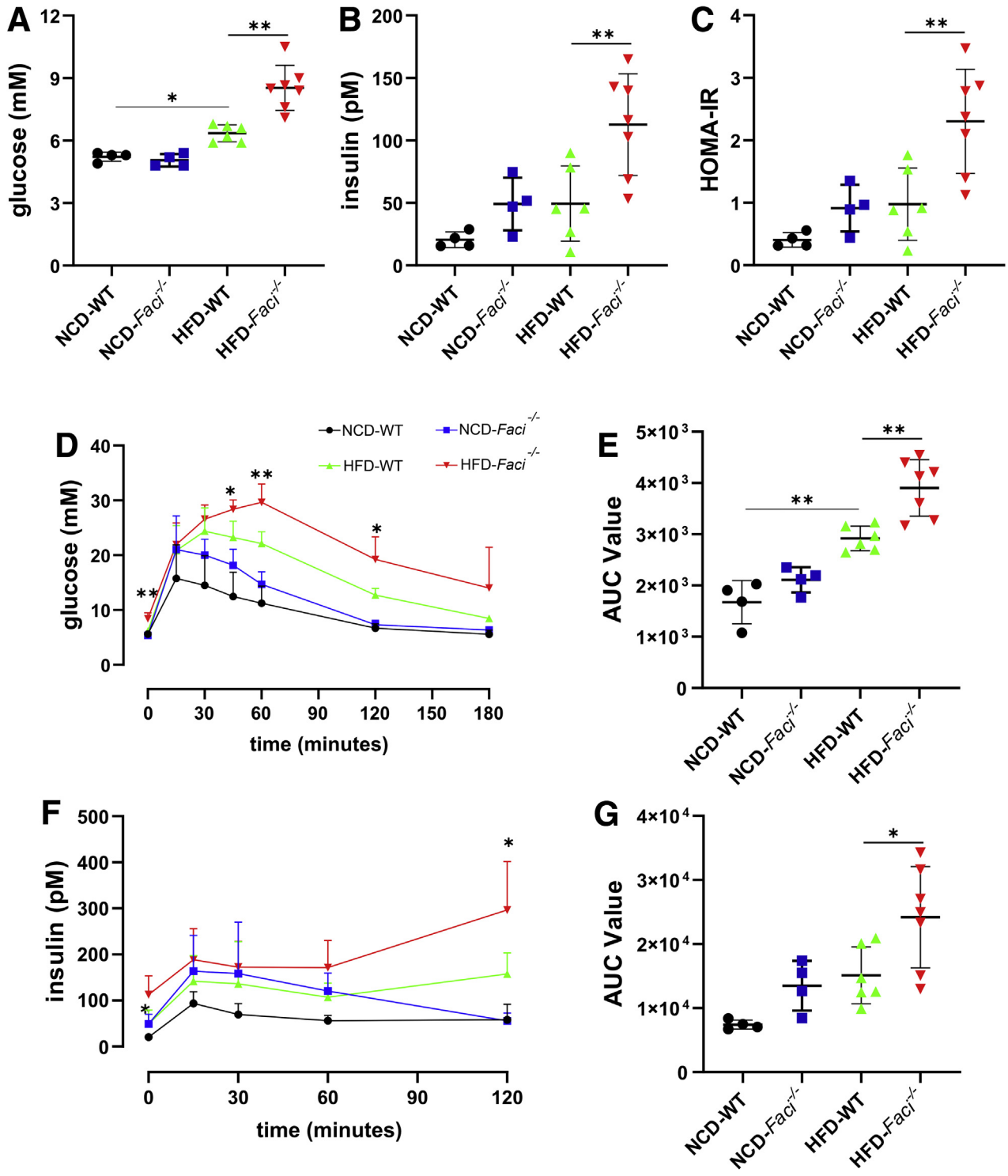

samples were collected at 0, 60, 120, 180, and 240 minutes after injection by tail bleeding. Plasma TG was examined by a reagent kit from Stanbio.

Intestinal TG Absorption

Male WT and *Faci*$^{-/-}$ mice (n = 4 per group) were HFD-fed for 5 days, fasted for 6 hours, and injected intraperitoneally with 30% wt/wt lipoprotein lipase inhibitor poloxamer 407 solution in PBS (1.5 g/kg body weight). After 30 minutes, mice were orally gavaged with olive oil (10 mL/g body weight). Blood samples were collected at 0, 60, 120, and 240 minutes after injection by tail bleeding. Plasma TG was examined by a reagent kit from Stanbio.

RNA Extraction and Real-Time RT-qPCR

Total RNA was extracted with RNAiso Plus reagent (Takara) according to the manufacturer's instructions. Extracted RNA was incubated with DNase I (Ambion Waltham, MA) at 37°C for 30 minutes to digest the remaining genomic DNA. Reverse-transcription was performed using the Transcriptor First-Strand Complementary DNA Synthesis reagents (Roche Basel, Switzerland).

SYBR green PCR master mix was purchased from Takara and real-time qPCR was conducted using StepOne Real-Time PCR system (Applied Biosystems Waltham, MA). Gene expression was normalized to β-tubulin by the $2^{-\Delta\Delta CT}$ method. The primer sequences used are listed in Supplementary Table 3.

RNA-seq

The total RNA from the intestinal epithelium of 4-month-old WT and *Faci*$^{-/-}$ mice (n = 3 per group) was extracted by RNAiso Plus reagent (Takara) and sent to the BGI Shenzhen Genomics Institute (Shenzhen, China) of for RNA sequencing. Briefly, RNA was quantified with a Nanodrop spectrophotometer (Thermo Scientific) and RNA integrity was verified with an Agilent Bioanalyzer 2100 system (Agilent Technologies, Santa Clara, CA). Libraries for RNA sequencing were prepared with standard protocol, which includes mRNA enrichment, reverse-transcription, bubble adaptor ligation, PCR amplification, and circular single-strand DNA generation. RNA sequencing was conducted on the BGISEQ-500 platform. The generated raw sequencing reads were filtered and mapped to the reference genome using HISAT.[68] The clean reads were aligned to reference transcripts with Bowtie2.[69] Gene expression levels were calculated with RSEM.[70] DEGs were identified with DEseq2.[71] Genes were considered significantly differentially expressed if fold change was 1 or greater and the adjusted *P* value was less than .05. Pathway enrichment analysis of DEGs was performed with gene ontology analysis. Data were deposited in the NCBI Gene Expression Omnibus under accession number GSE193731.

Protein Extraction and Immunoblotting

Immunoblotting was performed as described previously.[17] Cell or tissue samples were lysed in RIPA lysis buffer (25 mmol/L Tris-HCl, pH 7.4, 150 mmol/L NaCl, 1% NP-40, 0.1% sodium dodecyl sulfate, 0.5% sodium deoxycholate) supplemented with protease inhibitor cocktails (Roche) by a 30-minute incubation at 4°C. The protein concentration of lysates was measured with the Bradford dye-binding method (Bio-Rad Hercules, CA). Protein samples were separated by sodium dodecyl sulfate–polyacrylamide gel electrophoresis, electroblotted onto polyvinylidene difluoride membranes (Millipore Burlington, MA), incubated with primary and secondary antibodies sequentially, and visualized by enhanced chemiluminescence (Amersham Marlborough, MA).

Subcellular Fractionation Assay

Total membrane and cytosolic protein fractions of AML12-V5-FACI cells were isolated using the Minute Plasma Membrane Protein Isolation and Cell Fractionation Kit (Invent Biotechnologies, Eden Prairie, MN). The experimental procedures were as suggested by the manufacturer.

Dual-Luciferase Reporter Assay

The dual-luciferase reporter assay was performed as described previously.[17] The firefly luciferase expression plasmid pFACI-Luc (pW) and its mutant forms (pA, pB, and pC) with truncated promoter regions are listed in Supplementary Table 3. HepG2, Hep3B, and AML12 cells were seeded into 24-well culture plates and transfected with pFACI-Luc or its mutant forms together with a Renilla luciferase expressing plasmid (pSV-RLuc from Promega Madison, WI) as an internal control. Cells then were harvested 48 hours after transfection and lysed for luciferase activity analysis. Each transfection was performed in triplicate and the result was normalized to Renilla luciferase activity.

Figure 11. (***See previous page***). ***Faci* deficiency exacerbates insulin resistance in mice.** Overnight fasting (*A*) blood glucose, (*B*) blood insulin, and (*C*) homeostasis model assessment of the insulin resistance index (HOMA-IR) of male WT and *Faci*$^{-/-}$ mice on NCD or HFD diet for 11 weeks. Data were statistically analyzed with 1-way ANOVA with Tukey post hoc tests. The HOMA-IR values were calculated using iHOMA2 software. (*D* and *E*) Intraperitoneal glucose tolerance test (IPGTT) of male WT and *Faci*$^{-/-}$ mice on NCD or HFD diet for 11 weeks (4 mice per NCD group, 6 mice per HFD-WT group, and 7 mice per HFD-*Faci*$^{-/-}$ group). Mice were overnight-fasted and injected with 1 g/kg glucose intraperitoneally. The blood glucose levels were examined at regular intervals. Results were statistically analyzed by 2-way ANOVA with repeated measures followed by the Tukey test. (*E*) Areas under the curve (AUC) for IPGTT were calculated using Y = 0 as the baseline. Results were statistically analyzed by 1-way ANOVA with Tukey post hoc tests. (*F*) Blood insulin levels during IPGTT were examined and statistically assessed by 2-way ANOVA with repeated measures followed by the Tukey test. (*G*) The AUC was calculated using Y = 0 as the baseline and judged statistically by 1-way ANOVA with Tukey post hoc tests. **P* < .05, and ***P* < .01.

Immunofluorescent Staining

Cells were fixed with 4% paraformaldehyde in PBS for 15 minutes, permeabilized for 4 minutes with 0.1% Triton X-100 (Sigma, St. Louis, MO) in PBS, blocked with 3% BSA for 1 hour, and incubated with primary antibody overnight at 4°C sequentially. After washing, the cells were incubated with secondary antibodies conjugated with fluorophores (1:400) in a dark place at room temperature for 1 hour. The cells were further rinsed and then mounted with 4′,6-diamidino-2-phenylindole–containing mounting medium. Confocal images were acquired with the Confocal Laser Scanning Microscopes 780 or 880 (Zeiss Jena, Germany). Super-resolution images were acquired by Structured Illumination Microscopy (Zeiss ELYRA S1).

Histology, H&E Staining, and Pathologic Assessment

After mice were killed, liver tissues were obtained, fixed in 4% paraformaldehyde in PBS overnight at 4°C,

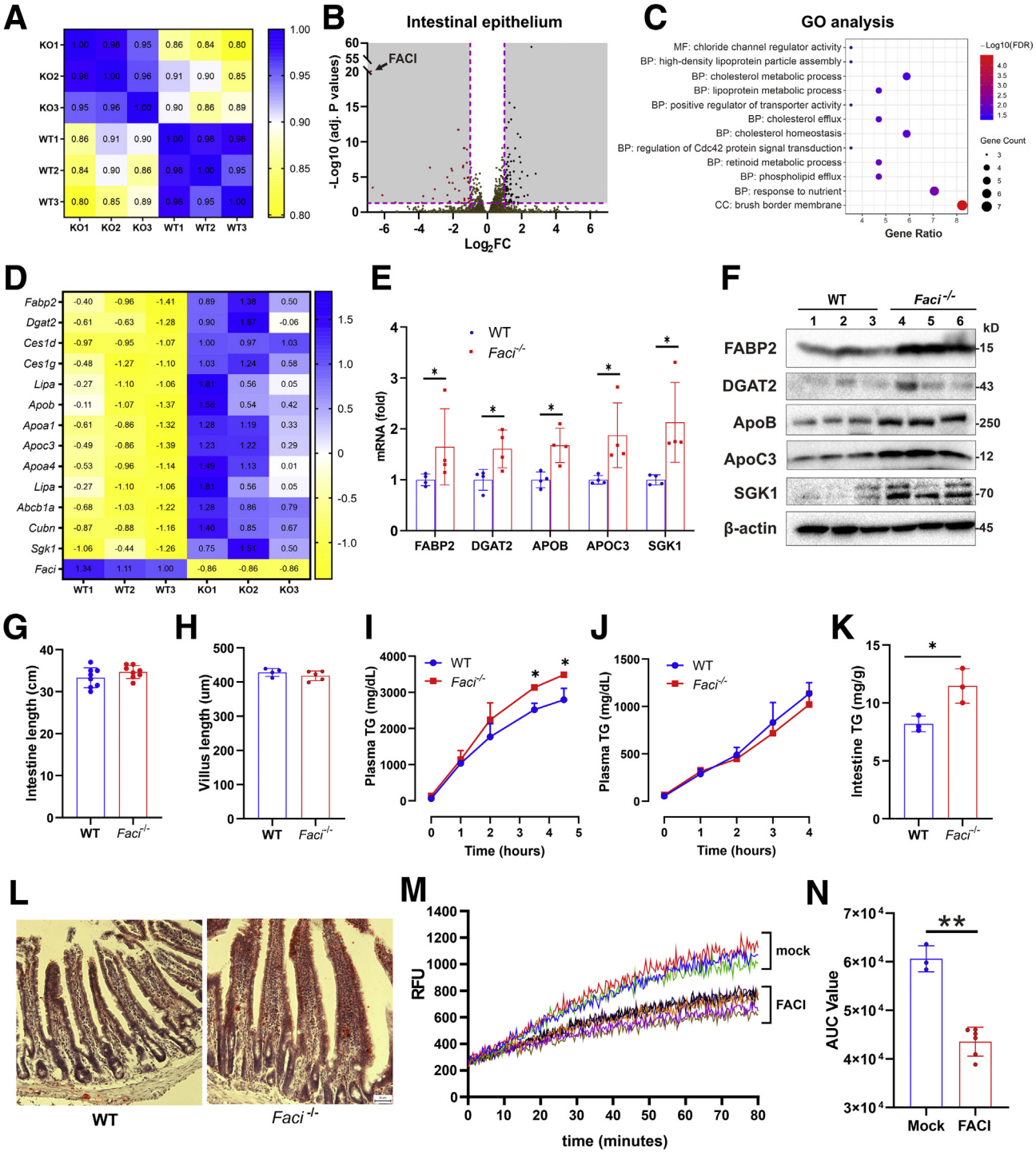

dehydrated in ethanol, and embedded in paraffin. Hepatic sections of 6 μm were made and stained with H&E. Images were taken using an Olympus BX51 microscope (Tokyo, Japan). The degree of steatosis was evaluated based on the previous histologic scoring system for nonalcoholic fatty liver disease.

Intestinal Villus Length Measurement

Small intestines dissected from mice were divided into 4 equal-length segments and immediately fixed by modified Bouin's fixative (50% ethanol and 5% acetic acid). The fixed intestinal segments then were opened longitutively, Swiss-rolled, fixed with 4% paraformaldehyde, and sectioned and stained with H&E. Images were taken and stitched using an Olympus BX51 Microscope and QuickPHOTO Micro software (Promicra, Prague, Czech). Intestinal villus length was measured as described.[72] Briefly, a full image of 1 section was divided into 4 quadrants. Ten intact villi were selected randomly from each quadrant and the villus lengths were measured from the villi apex to the distal edge of the crypt using ImageJ software (National Institutes of Health, Bethesda, MD). The mean villus length then was calculated, representing the corresponding small intestinal segments.

Oil Red O Staining

After mice were killed, the proximal jejunum and liver tissues were collected and completely washed in precooled PBS. The tissues were fixed in 4% paraformaldehyde for 16 hours at 4°C, dehydrated in 15% sucrose for 24 hours at 4°C, and embedded in Tissue-Tek OCT compound (Sakura Torrance, CA) at -80°C. Serial sections (10 μm) were cut, stained with 0.5% Oil Red O for 10 minutes to visualize neutral lipids, and stained with Mayer's hematoxylin to visualize nuclei. Images were taken under an Olympus BX51 microscope.

Fat Blot Assay

Membrane Lipid Strip (P-6002; Echelon Bioscience Salt Lake City, UT), PIP Strip (P-6001; Echelon Bioscience), and Sphingo Strip (P-6000; Echelon Bioscience) were used for fat blot assay. The experiments followed the manufacturer's protocol. Briefly, the strip was blocked with 1% skim milk in PBS at room temperature for 1 hour, followed by a 1-hour incubation with biotin-labeled FACI-C peptide (1 μg/mL in blocking buffer) or mock incubation at room temperature. The membrane then was washed and probed by HRP-conjugated streptavidin. The immunoblotting signals were analyzed by Gel Documentation Systems (Bio-Rad). Biotin-labeled FACI-C peptide was synthesized by GenScript. The peptide sequence is GDTEQLIQAQ RRGSRWWLRR YQQVRRRWES FVAIFPSVTL SQPASP (purity, >98%).

Lipid Extraction

Lipids were extracted from tissues following the Bligh and Dyer method.[73] Mouse liver tissues (50 mg) were homogenized in 360 μL cold PBS and mixed with 1 mL chloroform and 2 mL methanol. After vortex, the solution was

Figure 12. (***See previous page***). **Inhibition of intestinal lipid absorption by FACI.** (*A–D*) Transcriptomic profiles of intestinal epithelium from jejunum between WT and *Faci*$^{-/-}$ mice (male, n = 3) by RNA-seq analysis. (*A*) Heatmap depicting the correlation of 6 RNA-seq samples, that is, intestinal epithelium from 3 WT (WT1, WT2, and WT3) and 3 *Faci*$^{-/-}$ mice (KO1, KO2, and KO3) by Pearson correlation coefficient analyses. (*B*) The volcano plot illustrates DEGs. DEGs were selected with the criteria of FDR (false discovery rate) less than 0.01 and $\log_2$ (fold change) (FC) of 2 or greater. Up-regulated and down-regulated DEGs are shown in red and green, respectively. (C) The bubble plot depicts gene ontology of up-regulated DEGs. The Y-axis represents GO terms. The X-axis indicates the gene ratio. Bubble colors represent $\log_{10}$ (FDR) and bubble sizes indicate gene counts. (*D*) Heatmap illustrating the fold changes of lipid absorption–related DEGs in WT (WT1, WT2, and WT3) and *Faci*$^{-/-}$ mice (KO1, KO2, and KO3). Scaled FPKM values were used for heatmap generation (Supplementary Table 2). Up-regulation and down-regulation are highlighted in yellow and blue, respectively. (*E*) RT-qPCR analysis. Total mRNA of intestinal epithelium from jejunum of WT and *Faci*$^{-/-}$ mice (male, n = 4) was extracted. The mRNA levels of the indicated genes were analyzed by RT-qPCR. Results were statistically assessed by unpaired 2-tailed Student *t* test. (*F*) Immunoblotting. Total proteins of intestinal epithelium from jejunum of WT and *Faci*$^{-/-}$ mice (male, n = 3) were extracted. Expression of the indicated proteins was analyzed. β-actin was detected as the internal control. (*G*) Small intestine length of male WT and *Faci*$^{-/-}$ mice at 3 months (n = 18–20 mice per group). (*H*) Duodenum villus length of male WT and *Faci*$^{-/-}$ mice at 3 months (n = 4 per group). (*I*) Plasma TG measurement. Male mice (n = 4 per group) were HFD-fed for 5 days, fasted (6 hours), and injected intraperitoneally with 30% wt/wt lipoprotein lipase inhibitor poloxamer 407 (1.5 g/kg body weight). After 30 minutes, mice were orally gavaged with olive oil (10 mL/g body weight). Plasma TGs at the indicated time points were measured. Statistical analysis was based on 2-way ANOVA with repeated measures, followed by the Sidak test. (*J*) Very-low-density lipoprotein secretion assay. Female mice (n = 3 per group) were fed with HFD for 5 days, fasted overnight, and injected intraperitoneally with Poloxamer 407 (1.5 g/kg). Plasma TG was measured at the indicated time points. Data are shown as means ± SD. (*K*) Measurement of TG in small intestines. Male mice (n = 3 per group) were HFD-fed for 5 days, fasted overnight, followed by high-fat refeeding. Small intestines of mice were removed, washed, and homogenized. Lipids were extracted following the Bligh and Dyer method.[69] Statistical analysis was performed with an unpaired 2-tailed Student *t* test. (*L*) Oil red O staining of proximal jejunum. Male mice were HFD-fed for 5 days, fasted overnight, followed by high-fat refeeding. Intestinal neutral lipids were visualized with Oil red O staining. (*M* and *N*) Fatty acid uptake assay. BODIPY-C12 fatty acid uptake was measured using the QBT fatty acid uptake kit (Molecular Devices). (*M*) Intracellular fluorescence signals were detected every 20 seconds for up to 80 minutes. Fatty acid uptake was compared between FACI-expressing (Dox group, n = 6 wells) and mock-treated (no Dox group, n = 3 wells) Caco2 cells. (*N*) Areas under the curve (AUC) for kinetic FA uptake were calculated. An unpaired 2-tailed Student *t* test was performed to assess statistical significance. **P* < .05, ***P* < .01. adj, adjusted; BP, biological process; CC, cellular component; MF, molecular function; RFU, Relative fluorescence unit.

mixed with 1 mL chloroform, after which 1.4 mL of 0.88% NaCl solution was added. The mixtures were centrifuged further at 2000 $\times$ g for 15 minutes at 4°C. The organic phases containing lipids were dried and reconstituted in 200 μL of 2% Triton X-100 in H_2O. Liver TG and cholesterol levels were determined by commercial kits (Stanbio) and normalized to liver tissue weights.

For intestinal lipid extraction, overnight fasted mice were refed with HFD and killed. Entire small intestines were collected, completely washed, weighted, and homogenized. Intestinal lipids were extracted following the Bligh and Dyer method,[73] with the solvent system consisting of chloroform:methanol:water at 2:2:1.8 (vol/vol/vol).

In Vitro Fatty Acid Uptake

Fatty acid uptake was determined using the QBT fatty acid uptake kit (Molecular Devices San Jose, CA) according to the manufacturer's protocol. FACI-V5-Caco2 cells were seeded onto a clear-bottom, 24-well plate. After reaching approximately 80% confluence, cells were treated with 1 μg/mL doxycycline for 48 hours to induce FACI expression. Cells were prestarved with Eagle's minimum essential medium with 0.2% fatty acid–free BSA for 1 hour and then raised in 300 μL QBT fatty acid uptake solution for kinetic fluorescence reading. Fluorescence was monitored at 485-nm excitation/515-nm emission every 20 seconds for 80 minutes by Varioskan flash spectral scanning multimode readers (Thermo Scientific Waltham, MA).

Statistics

Results presented are means $\pm$ SD. The statistical analyses were performed using GraphPad Prism 8 San Diego, CA. All data were subjected to the Shapiro–Wilk test or the Kolmogorov–Smirnov test for normality assessment. Statistical analyses were performed with a 2-tailed unpaired Student t test or 1-way analysis of variance (ANOVA), followed by the Tukey post hoc comparison, unless otherwise stated. In detail, for normally distributed data with equal variances (2 groups), the 2-tailed Student t test was used. For normally distributed data with unequal variances (2 groups), the 2-tailed Student t test with the Welch correction was used. The 2-tailed Student t test also was applied for planned 2-group comparison. For normally distributed data sets with equal variances (>2 groups), 1-way ANOVA was used followed by the Tukey post hoc comparison or the Dunnett post hoc comparison. For normally distributed data sets with unequal variances (>2 groups), 1-way ANOVA with the Welch correction was used followed by Games Howell post hoc comparison. For non-normally distributed data sets, nonparametric tests were used. For data sets with 2 independent variables, 2-way ANOVA or 2-way ANOVA with repeated measures was used, followed by the Tukey or Sidak multiple comparison test as specified.

References

1. Ko CW, Qu J, Black DD, Tso P. Regulation of intestinal lipid metabolism: current concepts and relevance to disease. Nat Rev Gastroenterol Hepatol 2020;17:169–183.
2. Hussain MM. Intestinal lipid absorption and lipoprotein formation. Curr Opin Lipidol 2014;25:200–206.
3. Ros E. Intestinal absorption of triglyceride and cholesterol. Dietary and pharmacological inhibition to reduce cardiovascular risk. Atherosclerosis 2000;151:357–379.
4. Iqbal J, Hussain MM. Intestinal lipid absorption. Am J Physiol Endocrinol Metab 2009;296:E1183–E1194.
5. Xiao C, Stahel P, Carreiro AL, Buhman KK, Lewis GF. Recent advances in triacylglycerol mobilization by the gut. Trends Endocrinol Metab 2018;29:151–163.
6. Mansbach CM, Siddiqi SA. The biogenesis of chylomicrons. Annu Rev Physiol 2010;72:315–333.
7. Shimano H, Sato R. SREBP-regulated lipid metabolism: convergent physiology - divergent pathophysiology. Nat Rev Endocrinol 2017;13:710–730.
8. Lee AH. The role of CREB-H transcription factor in triglyceride metabolism. Curr Opin Lipidol 2012;23:141–146.
9. Lee JH, Giannikopoulos P, Duncan SA, Wang J, Johansen CT, Brown JD, Plutzky J, Hegele RA, Glimcher LH, Lee AH. The transcription factor cyclic AMP-responsive element-binding protein H regulates triglyceride metabolism. Nat Med 2011;17:812–815.
10. Chin KT, Zhou HJ, Wong CM, Lee JM, Chan CP, Qiang BQ, Yuan JG, Ng IO, Jin DY. The liver-enriched transcription factor CREB-H is a growth suppressor protein underexpressed in hepatocellular carcinoma. Nucleic Acids Res 2005;33:1859–1873.
11. Johansen CT, Wang J, McIntyre AD, Martins RA, Ban MR, Lanktree MB, Huff MW, Peterfy M, Mehrabian M, Lusis AJ, Kathiresan S, Anand SS, Yusuf S, Lee AH, Glimcher LH, Cao H, Hegele RA. Excess of rare variants in non-genome-wide association study candidate genes in patients with hypertriglyceridemia. Circ Cardiovasc Genet 2012;5:66–72.
12. Dron JS, Dilliott AA, Lawson A, McIntyre AD, Davis BD, Wang J, Cao H, Movsesyan I, Malloy MJ, Pullinger CR, Kane JP, Hegele RA. Loss-of-function CREB3L3 variants in patients with severe hypertriglyceridemia. Arterioscler Thromb Vasc Biol 2020;40:1935–1941.
13. Nakagawa Y, Shimano H. CREBH regulates systemic glucose and lipid metabolism. Int J Mol Sci 2018;19:1396.
14. Kikuchi T, Orihara K, Oikawa F, Han SI, Kuba M, Okuda K, Satoh A, Osaki Y, Takeuchi Y, Aita Y, Matsuzaka T, Iwasaki H, Yatoh S, Sekiya M, Yahagi N, Suzuki H, Sone H, Nakagawa Y, Yamada N, Shimano H. Intestinal CREBH overexpression prevents high-cholesterol diet-induced hypercholesterolemia by reducing Npc1l1 expression. Mol Metab 2016;5:1092–1102.
15. Nakagawa Y, Wang Y, Han SI, Okuda K, Oishi A, Yagishita Y, Kumagai K, Ohno H, Osaki Y, Mizunoe Y, Araki M, Murayama Y, Iwasaki H, Konishi M, Itoh N, Matsuzaka T, Sone H, Yamada N, Shimano H. Enterohepatic transcription factor CREB3L3 protects atherosclerosis via SREBP competitive inhibition. Cell Mol Gastroenterol Hepatol 2021;11:949–971.

16. Chan CP, Mak TY, Chin KT, Ng IO, Jin DY. N-linked glycosylation is required for optimal proteolytic activation of membrane-bound transcription factor CREB-H. J Cell Sci 2010;123:1438–1448.
17. Cheng Y, Gao WW, Tang HM, Deng JJ, Wong CM, Chan CP, Jin DY. β-TrCP-mediated ubiquitination and degradation of liver-enriched transcription factor CREB-H. Sci Rep 2016;6:23938.
18. Ruppert PMM, Park JG, Xu X, Hur KY, Lee AH, Kersten S. Transcriptional profiling of PPAR$\alpha^{-/-}$ and CREB3L3$^{-/-}$ livers reveals disparate regulation of hepatoproliferative and metabolic functions of PPARα. BMC Genomics 2019;20:199.
19. Schwartz AL, Fridovich SE, Knowles BB, Lodish HF. Characterization of the asialoglycoprotein receptor in a continuous hepatoma line. J Biol Chem 1981; 256:8878–8881.
20. Wu JC, Merlino G, Fausto N. Establishment and characterization of differentiated, nontransformed hepatocyte cell lines derived from mice transgenic for transforming growth factor alpha. Proc Natl Acad Sci U S A 1994; 91:674–678.
21. Aden DP, Fogel A, Plotkin S, Damjanov I, Knowles BB. Controlled synthesis of HBsAg in a differentiated human liver carcinoma-derived cell line. Nature 1979; 282:615–616.
22. Tabula Muris Consortium. Overall Coordination, Logistical Coordination, Organ Collection and Processing, Library Preparation and Sequencing, Computational Data Analysis, Cell Type Annotation, Writing Group, Supplemental Text Writing Group, Principal Investigators. Single-cell transcriptomics of 20 mouse organs creates a Tabula Muris. Nature 2018;562: 367–372.
23. Li X, Madison BB, Zacharias W, Kolterud A, States D, Gumucio DL. Deconvoluting the intestine: molecular evidence for a major role of the mesenchyme in the modulation of signaling cross talk. Physiol Genomics 2007;29:290–301.
24. Haber AL, Biton M, Rogel N, Herbst RH, Shekhar K, Smillie C, Burgin G, Delorey TM, Howitt MR, Katz Y, Tirosh I, Beyaz S, Dionne D, Zhang M, Raychowdhury R, Garrett WS, Rozenblatt-Rosen O, Shi HN, Yilmaz O, Xavier RJ, Regev A. A single-cell survey of the small intestinal epithelium. Nature 2017;551:333–339.
25. Beacham GM, Partlow EA, Hollopeter G. Conformational regulation of AP1 and AP2 clathrin adaptor complexes. Traffic 2019;20:741–751.
26. Park SY, Guo X. Adaptor protein complexes and intracellular transport. Biosci Rep 2014;34:e00123.
27. Grasset E, Pinto M, Dussaulx E, Zweibaum A, Desjeux JF. Epithelial properties of human colonic carcinoma cell line Caco-2: electrical parameters. Am J Physiol 1984;247:C260–C267.
28. Hubbard WC, Alley MC, McLemore TL, Boyd MR. Evidence for thromboxane biosynthesis in established cell lines derived from human lung adenocarcinomas. Cancer Res 1988;48:2674–2677.
29. Nakamura N, Rabouille C, Watson R, Nilsson T, Hui N, Slusarewicz P, Kreis TE, Warren G. Characterization of a cis-Golgi matrix protein, GM130. J Cell Biol 1995; 131:1715–1726.
30. van der Klei IJ, Hilbrands RE, Swaving GJ, Waterham HR, Vrieling EG, Titorenko VI, Cregg JM, Harder W, Veenhuis M. The Hansenula polymorpha PER3 gene is essential for the import of PTS1 proteins into the peroxisomal matrix. J Biol Chem 1995;270:17229–17236.
31. Smith MJ, Koch GL. Multiple zones in the sequence of calreticulin (CRP55, calregulin, HACBP), a major calcium binding ER/SR protein. EMBO J 1989;8:3581–3586.
32. Dahlhoff M, Camera E, Picardo M, Zouboulis CC, Chan L, Chang BH, Schneider MR. PLIN2, the major perilipin regulated during sebocyte differentiation, controls sebaceous lipid accumulation in vitro and sebaceous gland size in vivo. Biochim Biophys Acta 2013; 1830:4642–4649.
33. Lee SA, Eyeson R, Cheever ML, Geng J, Verkhusha VV, Burd C, Overduin M, Kutateladze TG. Targeting of the FYVE domain to endosomal membranes is regulated by a histidine switch. Proc Natl Acad Sci USA 2005; 102:13052–13057.
34. Langemeyer L, Frohlich F, Ungermann C. Rab GTPase function in endosome and lysosome biogenesis. Trends Cell Biol 2018;28:957–970.
35. du Toit A, Hofmeyr JS, Gniadek TJ, Loos B. Measuring autophagosome flux. Autophagy 2018;14:1060–1071.
36. Gautier R, Douguet D, Antonny B, Drin G. HELIQUEST: a web server to screen sequences with specific alpha-helical properties. Bioinformatics 2008;24:2101–2102.
37. Gimenez-Andres M, Copic A, Antonny B. The many faces of amphipathic helices. Biomolecules 2018;8:45.
38. Chisari M, Saini DK, Cho JH, Kalyanaraman V, Gautam N. G protein subunit dissociation and translocation regulate cellular response to receptor stimulation. PLoS One 2009;4:e7797.
39. Ariotti N, Hall TE, Rae J, Ferguson C, McMahon KA, Martel N, Webb RE, Webb RI, Teasdale RD, Parton RG. Modular detection of GFP-labeled proteins for rapid screening by electron microscopy in cells and organisms. Dev Cell 2015;35:513–525.
40. Varnai P, Balla T. Visualization of phosphoinositides that bind pleckstrin homology domains: calcium- and agonist-induced dynamic changes and relationship to myo-[3H]inositol-labeled phosphoinositide pools. J Cell Biol 1998;143:501–510.
41. Toth JI, Datta S, Athanikar JN, Freedman LP, Osborne TF. Selective coactivator interactions in gene activation by SREBP-1a and -1c. Mol Cell Biol 2004;24:8288–8300.
42. Guo S, Lu H. Novel mechanisms of regulation of the expression and transcriptional activity of hepatocyte nuclear factor 4alpha. J Cell Biochem 2019; 120:519–532.
43. Tang HM, Gao WW, Chan CP, Cheng Y, Chaudhary V, Deng JJ, Yuen KS, Wong CM, Ng IO, Kok KH, Zhou J, Jin DY. Requirement of CRTC1 coactivator for hepatitis B virus transcription. Nucleic Acids Res 2014; 42:12455–12468.
44. Gao WW, Tang HV, Cheng Y, Chan CP, Chan CP, Jin DY. Suppression of gluconeogenic gene transcription by SIK1-induced ubiquitination and degradation of

CRTC1. Biochim Biophys Acta Gene Regul Mech 2018;1861:211–223.
45. Ichida M, Nemoto S, Finkel T. Identification of a specific molecular repressor of the peroxisome proliferator-activated receptor γ coactivator-1α (PGC-1α). J Biol Chem 2002;277:50991–50995.
46. Rui L. Energy metabolism in the liver. Compr Physiol 2014;4:177–197.
47. Tran KV, Brown EL, DeSouza T, Jespersen NZ, Nandrup-Bus C, Yang Q, Yang Z, Desai A, Min SY, Rojas-Rodriguez R, Lundh M, Feizi A, Willenbrock H, Larsen TJ, Severinsen MCK, Malka K, Mozzicato AM, Deshmukh AS, Emanuelli B, Pedersen BK, Fitzgibbons T, Scheele C, Corvera S, Nielsen S. Human thermogenic adipocyte regulation by the long noncoding RNA LINC00473. Nat Metab 2020;2:397–412.
48. Petersen MC, Shulman GI. Mechanisms of insulin action and insulin resistance. Physiol Rev 2018;98:2133–2223.
49. Dash S, Xiao C, Morgantini C, Lewis GF. New insights into the regulation of chylomicron production. Annu Rev Nutr 2015;35:265–294.
50. Matschke J, Wiebeck E, Hurst S, Rudner J, Jendrossek V. Role of SGK1 for fatty acid uptake, cell survival and radioresistance of NCI-H460 lung cancer cells exposed to acute or chronic cycling severe hypoxia. Radiat Oncol 2016;11:75.
51. Dieter M, Palmada M, Rajamanickam J, Aydin A, Busjahn A, Boehmer C, Luft FC, Lang F. Regulation of glucose transporter SGLT1 by ubiquitin ligase Nedd4-2 and kinases SGK1, SGK3, and PKB. Obes Res 2004;12:862–870.
52. von Heijne G. Membrane-protein topology. Nat Rev Mol Cell Biol 2006;7:909–918.
53. Oldfield CJ, Dunker AK. Intrinsically disordered proteins and intrinsically disordered protein regions. Annu Rev Biochem 2014;83:553–584.
54. Zanzoni A, Ribeiro DM, Brun C. Understanding protein multifunctionality: from short linear motifs to cellular functions. Cell Mol Life Sci 2019;76:4407–4412.
55. Arencibia JM, Pastor-Flores D, Bauer AF, Schulze JO, Biondi RM. AGC protein kinases: from structural mechanism of regulation to allosteric drug development for the treatment of human diseases. Biochim Biophys Acta 2013;1834:1302–1321.
56. O'Sullivan MJ, Lindsay AJ. The endosomal recycling pathway-At the crossroads of the cell. Int J Mol Sci 2020;21:6074.
57. Grant BD, Donaldson JG. Pathways and mechanisms of endocytic recycling. Nat Rev Mol Cell Biol 2009;10:597–608.
58. Wang B, Rong X, Duerr MA, Hermanson DJ, Hedde PN, Wong JS, Vallim TQ, Cravatt BF, Gratton E, Ford DA, Tontonoz P. Intestinal phospholipid remodeling is required for dietary-lipid uptake and survival on a high-fat diet. Cell Metab 2016;23:492–504.
59. Sierra-Ramos C, Velazquez-Garcia S, Vastola-Mascolo A, Hernandez G, Faresse N, Alvarez de la Rosa D. SGK1 activation exacerbates diet-induced obesity, metabolic syndrome and hypertension. J Endocrinol 2020;244:149–162.
60. Kopin L, Lowenstein C. Dyslipidemia. Ann Intern Med 2017;167:ITC81–ITC96.
61. Goldman MJ, Craft B, Hastie M, Repecka K, McDade F, Kamath A, Banerjee A, Luo Y, Rogers D, Brooks AN, Zhu J, Haussler D. Visualizing and interpreting cancer genomics data via the Xena platform. Nat Biotechnol 2020;38:675–678.
62. Byun J, Schwartz AG, Lusk C, Wenzlaff AS, de Andrade M, Mandal D, Gaba C, Yang P, You M, Kupert EY, Anderson MW, Han Y, Li Y, Qian D, Stilp A, Laurie C, Nelson S, Zheng W, Hung RJ, Gaborieau V, McKay J, Brennan P, Caporaso NE, Landi MT, Wu X, McLaughlin JR, Brhane Y, Bosse Y, Pinney SM, Bailey-Wilson JE, Amos CI. Genome-wide association study of familial lung cancer. Carcinogenesis 2018;39:1135–1140.
63. Kiernan R, Brès V, Ng RW, Coudart MP, El Messaoudi S, Sardet C, Jin DY, Emiliani S, Benkirane M. Post-activation turn-off of NF-κB-dependent transcription is regulated by acetylation of p65. J Biol Chem 2003;278:2758–2766.
64. Deng JJ, Kong KE, Gao WW, Tang HV, Chaudhary V, Cheng Y, Zhou J, Chan CP, Wong DK, Yuen MF, Jin DY. Interplay between SIRT1 and hepatitis B virus X protein in the activation of viral transcription. Biochim Biophys Acta Gene Regul Mech 2017;1860:491–501.
65. Cunningham SC, Dane AP, Spinoulas A, Alexander IE. Gene delivery to the juvenile mouse liver using AAV2/8 vectors. Mol Ther 2008;16:1081–1088.
66. Zeineldin M, Neufeld K. Isolation of epithelial cells from mouse gastrointestinal tract for Western blot or RNA analysis. Bio Protoc 2012;2:e292.
67. Hill NR, Levy JC, Matthews DR. Expansion of the homeostasis model assessment of beta-cell function and insulin resistance to enable clinical trial outcome modeling through the interactive adjustment of physiology and treatment effects: iHOMA2. Diabetes Care 2013;36:2324–2330.
68. Kim D, Langmead B, Salzberg SL. HISAT: a fast spliced aligner with low memory requirements. Nat Methods 2015;12(4):357–360.
69. Langmead B, Salzberg SL. Fast gapped-read alignment with Bowtie 2. Nat Methods 2012;9(4):357–359.
70. Li B, Dewey CN. RSEM: accurate transcript quantification from RNA-Seq data with or without a reference genome. BMC Bioinformatics 2011;12:323.
71. Love MI, Huber W, Anders S. Moderated estimation of fold change and dispersion for RNA-seq data with DESeq2. Genome Biol 2014;15(12):550.
72. Taylor SR, Ramsamooj S, Liang RJ, Katti A, Pozovskiy R, Vasan N, Hwang SK, Nahiyaan N, Francoeur NJ, Schatoff EM, Johnson JL, Shah MA, Dannenberg AJ, Sebra RP, Dow LE, Cantley LC, Rhee KY, Goncalves MD. Dietary fructose improves intestinal cell survival and nutrient absorption. Nature 2021;597:263–267.
73. Sündermann A, Eggers LF, Schwudke D. Liquid extraction: Bligh and Dyer. In: Wenk MR, ed. Encyclopedia of lipidomics. Dordrecht: Springer Netherlands, 2016:1–4.

Received September 2, 2021. Accepted January 19, 2022.

Correspondence
Address correspondence to: Dong-Yan Jin, or Yun Cheng, PhD, School of Biomedical Sciences, The University of Hong Kong, 3/F Lab Block, 21 Sassoon Road, Pokfulam, Hong Kong. e-mail: yuncheng@hku.hk; dyjin@hku.hk; fax: (852) 28551254.

Acknowledgments
The authors thank the Center for PanorOmic Sciences of the University of Hong Kong for maintaining the PMCore liquid chromatography with tandem mass spectrometry (LC-MS/MS) service and providing technical support to our mass spectrometric analysis, HKUMed core facility for assistance with flow cytometry and confocal microscopy, and State Key Laboratory of Pharmaceutical Biotechnology of the University of Hong Kong for providing facilities for animal phenotyping. The authors also thank members of the Jin Laboratory for their comments and suggestions on earlier versions of the manuscript.

Data Availability
The RNA-seq data set has been deposited in NCBI GEO.

CRediT Authorship Contributions
Yun Cheng (Conceptualization: Lead; Data curation: Lead; Formal analysis: Lead; Funding acquisition: Equal; Investigation: Lead; Methodology: Lead; Project administration: Equal; Resources: Supporting; Supervision: Supporting; Validation: Equal; Writing – original draft: Lead; Writing – review & editing: Lead)

Xiao-Zhuo Kang (Data curation: Supporting; Investigation: Supporting)

Tao Cheng (Investigation: Supporting)

Zi-Wei Ye (Data curation: Supporting; Formal analysis: Supporting; Investigation: Supporting)

George L. Tipoe (Conceptualization: Supporting; Supervision: Supporting)

Cheng-han Yu (Data curation: Supporting; Resources: Supporting; Supervision: Equal; Writing – review & editing: Supporting)

Chi-Ming Wong (Conceptualization: Supporting; Methodology: Supporting; Resources: Supporting; Supervision: Supporting)

Baohua Liu (Data curation: Supporting; Funding acquisition: Supporting; Resources: Equal)

Chi-Ping Chan (Conceptualization: Supporting; Data curation: Supporting; Resources: Supporting; Writing – review & editing: Supporting)

Dong-Yan Jin, (Conceptualization: Equal; Data curation: Supporting; Formal analysis: Supporting; Funding acquisition: Lead; Project administration: Lead; Resources: Lead; Supervision: Lead; Writing – original draft: Supporting; Writing – review & editing: Lead)

Conflicts of interest
The authors disclose no conflicts.

Funding
Supported by research grants 05163786 (Y.C.) and 08193856 (D.-Y.J.) from the Hong Kong Health and Medical Research Fund.